# Colored Coded Aperture Design for Compressive Spectral Unmixing

**Héctor Miguel Vargas García**

**Universidad Industrial de Santander**
**Facultad de Ingenierías Físico-mecánicas**
**Escuela de Ingeniería Eléctrica, Electrónica y Telecomunicaciones**
**Maestría en Ingeniería Electróncia**
**Bucaramanga, 2016**

# Colored Coded Aperture Design for Compressive Spectral Unmixing

**Héctor Miguel Vargas García**
Cod: **2148772**

Trabajo de Investigación para optar por el título de:
**Magíster en Ingeniería Electrónica**

Director: **Henry Arguello Fuentes**

**Universidad Industrial de Santander**
**Facultad de Ingenierías Físico-mecánicas**
**Escuela de Ingeniería Eléctrica, Electrónica y Telecomunicaciones**
**Maestría en Ingeniería Electróncia**
**Bucaramanga, 2016**

# Contents

# Resumen

**TÍTULO:** Diseño de códigos de color para la separación de imágenes espectrales desde un conjunto de medidas comprimidas. [1]

**AUTOR:** Héctor Miguel Vargas Garcia.[2]

**PALABRAS CLAVE:** Códigos de Color, imágenes espectrales, muestreo compresivo, aperturas codificadas.

**DESCRIPCIÓN:**

Debido a los grandes volúmenes de datos recopilados por sensores espectrales, las investigaciones en técnicas de compresión de datos espectrales ha crecido exponencialmente. En muestreo remoto, las plataformas satelitales/aéreas recogen información espectral que luego es enviada a estaciones terrestres para su posterior procesamiento como la separación espectral. El reducido canal de comunicación entre la plataforma satélite/aérea y la estación de tierra limita la cantidad de datos que pueden transmitidos. Para esto, las técnicas de reducción de dimensión pueden ser útiles, operando sobre los datos en el subespacio de la señal, lo cual es computacionalmente económico y poco espacio de almacenamiento es necesario. Sin embargo, estas técnicas requieren la colección de datos completa descartando la información redundante que se adquirió en el proceso de muestreo. En este trabajo se ha propuesto un modelo de mezcla lineal espectral en un sistema de imágenes espectrales compresivas. El modelo propuesto dice que cada píxel espectral tiene una representación de pocos coeficientes en una librería espectral de pixeles puros. El vector de pocos coeficientes se estimado resolviendo un problema de optimización condicionado y métodos de variables separables. Resultados numéricos demuestran que las separación espectral es exitosa utilizando porcentajes de medidas alrededor del 10 y el 25% de toda la información espectral de la escena.

[1] Trabajo de Investigación

[2] Facultad de Ingenierías Fisicomecánicas. Escuela de Ingeniería Eléctrica, Electrónica y Telecomunicaciones. Director, PhD. Henry Arguello Fuentes.

# Abstract

**TITLE:** : Colored Coded Aperture Design for Compressive Spectral Unmixing [3]

**AUTHOR:** Héctor Miguel Vargas Garcia.[4]

**KEYWORDS:** Spectral imaging, compressive sensing, coded apertures, spectral unmixing.

**DESCRIPTION:**

Large volumes of data are collected by spectrometer systems and spectral data compression techniques are needed. RS on satellite/airborne platform collects spectral information and sends to it a ground station on Earth for subsequent processing. The communication channel between the satellite/airborne platform and the ground station is reduced, which limits the amount of data that can be transmitted. For this, DR can be very advantageous, operating on the data in the signal subspace is much less computationally intensive and less data storage. However, DR requires full data cube discarding redundant information that was acquired in the sensing process. In this work, a linear mixture model into compressive spectral imaging system has been used, which find the unmixed set of abundance maps from a set of compressive measures. The proposed scheme exploits that every spectral pixel is sparse in known spectral library of endmembers. The sparse vector is recovered solving a sparse nonnegative least square problem based augmented direction method of multiplier. Numerical results clearly demonstrate that compressively acquired data of size ranging from 10% to 25% of the full size can produce satisfactory results.

[3]Research Work

[4]2School of Physical-Mechanical Engineering. Department of Electrical, Electronic and Telecommunication Engineering. Advisor, PhD. Henry Arguello Fuentes

# Introduction

The acquisition of spectral images is the collection of information throughout the electromagnetic spectrum, dividing the information in images, where each image represents a range of the spectrum. These images are combined forming a three-dimensional spectral data cube, which is used for processing and analyzing of objects or scenes [1, 2]. The spectral and spatial high-resolution enables the identification of materials through signal processing techniques that provide a number of applications. However, having high spectral and spatial resolution comes with a price: The high volumes of data makes acquisition, transmission, storage and computational resource for data analysis. Also, the limitations of the actual sensors are a serious drawback due to the sensors only offering a high spatial resolution with a low spectral resolution or vice versa. There is a trade-off in spectral and spatial resolution and new advanced approaches for optimal data acquisition used in remote sensing is needed.

Traditional satellite remote sensing systems have spatial low resolution causing each pixel to be a mixture of several materials [3]. This work intends to use the concepts of Compressive Spectral Imaging Systems (CSI) based coded apertures (used for the acquisition of spectral images) [4] (CA), in order to reduce the number of acquisitions and performing spectral unmixing. For this, it is assumed that the spectral data cube has a representation with few coefficients that are different from zero (sparse) on some basis or at some dictionary. The main novelty of this research is in the use of Colored Coded Apertures (CCA) which have not been proposed for spectral unmixing. Also, unmixing and reconstruction are performed in one step by assuming that the spectral signatures involved are known.

First, the theoretical framework which integrates the theoretical approaches, studies and history in general with relation to the problem of research is presented. Second, the problem is addressed in this research, its problem statement, problem formulation, optimisation scheme. Finally, the results and conclusions are presented.

# 1

# Concepts

This chapter introduces spectral images, the concept of spatial an spectral resolution is explained. Remote Sensing, its relationship to spectral unmixing is discussed and main approaches used in dimensionality reduction are reviewed. The chapter concludes with the goals and novelties of the work presented here, along with an overview of the thesis.

## 1.1 Spectral Images (SI)

The Spectral Images (SI) are a set of data consisting of spatial and spectral information. The spectral information represents the response to the absorption or emission of electromagnetic radiation to certain wavelengths with spatial coordinates. These images are captured by spectrometry systems that measure the intensity of light waves to study the interaction of electromagnetic radiation with matter to analyse their characteristics. As shown in Figure 1.1, each record is associated with a coordinate system that creates a function $f(x_i, y_i, \lambda_k)$, where $(x, y)$ are the spatial coordinates and $(\lambda)$ is the spectral coordinate.

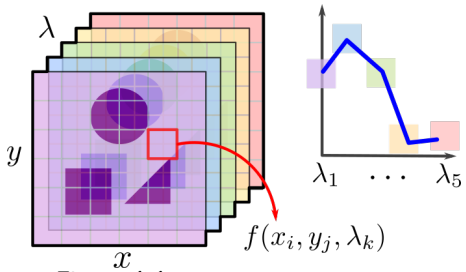


**Figure 1.1:** Spectral image concept.

The SI are used primarily in applications involving the detection, classification or identification of objects or properties based on their spectral characteristics in applications as agriculture [5], environment [6], pharmacology, among others [7].

**Spatial resolution:** This refers to the ability to distinguish features in an image and it can be expressed as the minimum distance by which two separate objects are perceived as disjoint. In the optical image sensors, the spatial resolution is generally related to the field of view (FOV) of the sensor [8]. Scene elements located at different positions FOV show

a different spatial resolution. This last aspect is very important for airborne platforms (large FOV) and negligible for satellite sensors (small FOV).

**Spectral resolution:** Spectral resolution is the ability of a sensor to respond to a range of specific wavelengths (spectral bands). As shown in Figure 1.2, the sensors can be classified as panchromatic (PAN), multispectral (MS), hyperspectral (HS). The PAN sensors work in a band. The best example are the sensors using the visible spectral range and near-infrared (NIR-V), where the detector is typically in the range of [400-1000] nanometers. The MS sensors operate in multiple wavelength ranges. The number of bands used is 3-10 in the visible range with wavelengths ranges of about 50 nanometers. When the spectral resolution is better than 10 nanometers, the sensors are denoted as HS and may contain hundreds of bands [8].

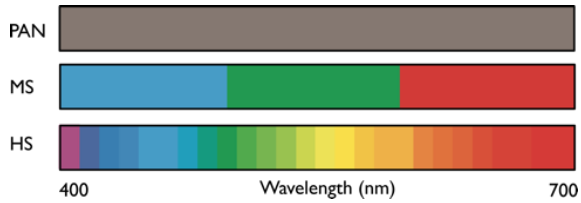


**Figure 1.2:** Classification of sensors based on spectral bandwidth. PAN, MS and HS denote panchromatic, multispectral and hyperspectral respectively.

## 1.2 Remote Sensing (RS)

Remote sensing (RS) has been defined as measuring, analyzing, and interpreting the spectra acquired from a given scene at a short, medium or long distance by an airborne or satellite sensor [9]. The airborne sensors measure the radiance that reflects from the ground and cover the visible, near-infrared and shortwave spectral bands (0.3$\mu$m to 2.5$\mu$m). The spatial and spectral resolution varies between sensors, and developers are constantly improving these sensors so the quality is improved and the resolution is increased.

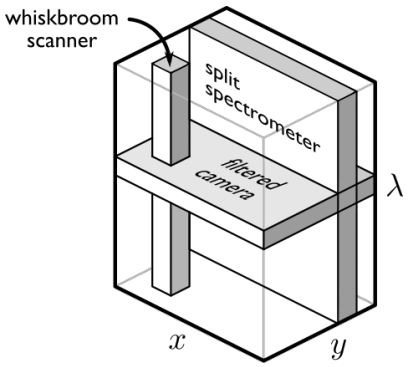


**Figure 1.3:** The hypercube that is sampled by traditional spectral imaging devices through spatial or spectral scanning.

**Acquisition methods:** An illustration of three acquisition methods is depicted in Figure 1.3. Two spatially scanned approaches: the slit spectrometer and [10] whiskbroom scanner [11]. These are scanned over the spatial dimensions $(x, y)$ of a scene to measure the 3-dimensional (3D) hypercube $(x, y, \lambda)$. Consequently, the spatial measurement is susceptible to temporal misregistration due to motion in the object or scene. Also spectral

scanned spectrometer: the filtered camera [2]. This sensor measures the wavelength ($\lambda$) by time-sequentially changing a spectral bandpass filter. Therefore, unlike the spatially scanned modalities, the spectral measurement is susceptible to temporal misregistration. Other acquisition methods may have different types of spatial artifacts dependent on the imaging method.

## 1.3 Spectral Unmixing (SU)

The sensors capture scenes in which a single pixel can contain spectral information of different materials. In remote sensing it is very common that more than one material can be within the spatial boundaries of one pixel. The spatial coordinates that contain multiple material are called mixed pixels, in contrast to pure pixels (PP) that are pixels containing only one material [12]. Figure 1.4 illustrates this. Each pixel in the grid is thus a sum of spectral reflectances from the different materials within the spatial boundaries of the pixel.

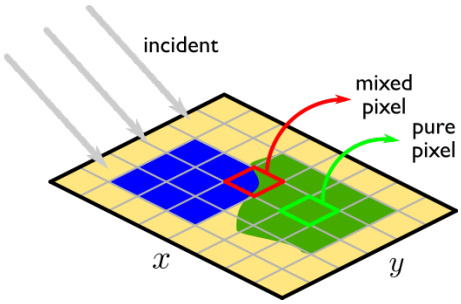


**Figure 1.4:** An illustration of the mixing process. The blue, yellow and green areas represent different material on the ground surface. The grid represents the resolution of the sensor. Some of the pixels may be mixed pixels while others may be pure.

**Unmixing:** The problem of spectral separation of mixed pixels is known in the literature as unmixing. Unmixing seeks to identify the components present in these mixed pixel and the spectrum measured in a mixed pixel is decomposed into a collection of spectral called endmembers [12]. In addition, the set of respective fractions or proportions of each spectrum in the pixel are called abundances. The unmixing process decomposes a mixed pixel, in a combination of materials or spectra and their abundances or proportions. As example, the Figure 1.4 shows the stages for spectral unmixing. After the acquiring data stage, the dimensionality reduction (DR) stage is used by assuming that the rank of data cube is equal to the number of endmembers. The objective of next stage is to determine the constituent spectral (unmixing). Several algorithms have been proposed for spectral unmixing [3]. Those methods are often categorized into geometrical, statistical, and sparse regression based methods [13]:

- Geometrical approaches assume that the spectral vectors are positioned in a simplex set or in a positive cone.
- Statistical approaches use parameter estimation methods to identify the endmember and abundance parameters.
- Sparse regression methods assume that the abundances are sparse and formulate the task as a sparse regression problem. These methods rely on spectral dictionaries

The last stage is the inversion. The inversion methods [14, 15] are based on minimizing square error. Advanced methods increase in complexity as further assumption and parametric structure are imposed on the problem as Full Additivity and Nonnegativity.

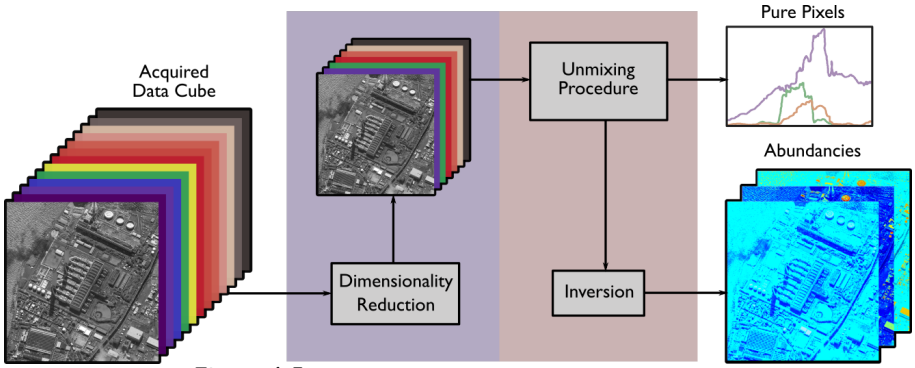


**Figure 1.5:** Stages for spectral separation (Unmixing).

## 1.4 Motivation

Large volumes of data are collected by spectrometer systems and spectral data compression techniques are needed [16, 17]. RS on satellite/airborne platform collects spectral information and sends to it a ground station on Earth for subsequent processing. The communication channel between the satellite/airborne platform and the ground station is reduced, which limits the amount of data that can be transmitted. For this, DR can be very advantageous, operating on the data in the signal subspace is much less computationally intensive and less data storage. However, DR requires full data cube discarding redundant information that was acquired in the sensing process. The next chapter will present the compressive sensing (CS) framework [18, 19] for acquisition of SI based on coded aperture [4, 20].

# 2

# Compressive Spectral Imaging System (CSI)

Traditional approaches to sampling signals and images are based on the Nyquist / Shannon theorem which states that the sampling rate must be greater than twice the bandwidth of an input signal [21]. However, in [22], a new concept called Compressive Sampling (CS) was proposed as a acquisition and compression method of signals. Generally, CS states that it is possible to obtain images or signals from a reduced number of data samples than the criterion of Nyquist / Shannon [23, 24, 25]. The success of this technique is that sensing and compression processes are carried out simultaneously and the number of samples required is significantly reduced. CS requires two conditions under which recovery is possible [26]. The first one is sparsity which requires the signal to be sparse in some domain. The second one is incoherence which is applied through the isometric property which is sufficient for sparse signals.

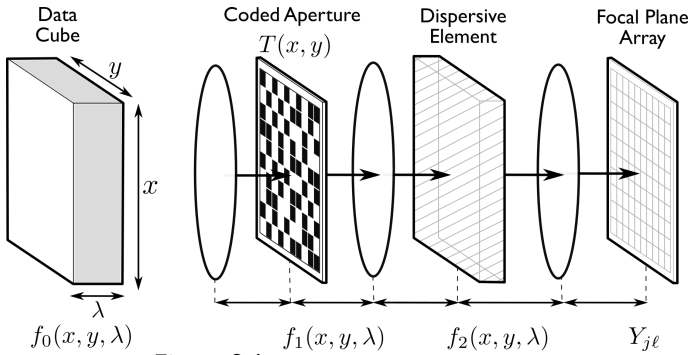


**Figure 2.1:** CASSI system architecture.

## 2.1 Discrete Model of CSI

One snapshot imaging is the Coded Aperture Snapshot Spectral Imaging (CASSI) that captures an approximation of the full spectral scene with a single snapshot [4]. The CASSI system, which is depicted in the Figure 2.1, simultaneously encodes spatial and spectral information of a scene in a small set of coded focal plane array (FPA) compressive measurements. In the CASSI system, the coding is applied to the image source density $f_0(x, y, \lambda)$ by the coded aperture $T(x, y)$, where $(x, y)$ are the spatial coordinates, and $\lambda$ is the wavelength. The resulting coded density $f_1(x, y)$ is spectrally dispersed by a dispersive

element before it impinges in the FPA, resulting in

$$f_2(x, y, \lambda) = \int \int T(x', y') f_0(x', y', \lambda) h(x' - S(\lambda) - x, y' - y) dx' dy' \tag{2.1}$$

where $h(x' - S(\lambda) - x, y' - y)$ is the optical impulse response of the system, and $S(\lambda)$ is the dispersion induced by a prism where linear dispersion is assumed. The compressive measurements across the FPA are obtained by the integration of the field $f_2(x, y)$ over the detector's spectral range. The discretized output at the detector can be thus modeled as

$$Y_{j\ell} = \sum_{l=0}^{L-1} F_{j(\ell+l)l} T_{j(\ell+l)} + \omega_{j\ell} \tag{2.2}$$

where $Y_{i\ell}$ is the intensity measured at the $(j, \ell)$ position of the detector whose dimensions are $N \times (N + L-1)$, $N \times N$ is the number of spatial pixels, $L$ is the number of spectral bands, $T_{j(\ell+l)}$ is the binary coded aperture, and $w_{j\ell}$ is the noise of the system. From Figure 2.2, CASSI blocks the light with one coded aperture and disperses incoming light with a prism. An intensity sensor measures the resulting multiplexed spatial and spectral information of the entire scene. Finally, an iterative method is used to reconstruct of the spectral data cube using CS measurements. The number of measurements is usually much smaller than the number of components of the original data cube. The single-shot CASSI system has been extended to a multishot system architecture such that multiframe coded measurements are acquired as separate FPA measurements, each with a distinct coded-aperture pattern that remains fixed during the integration time of the detector [27, 20, 28]. The multiple coded aperture can be implemented by a digital micromirror device (DMD).

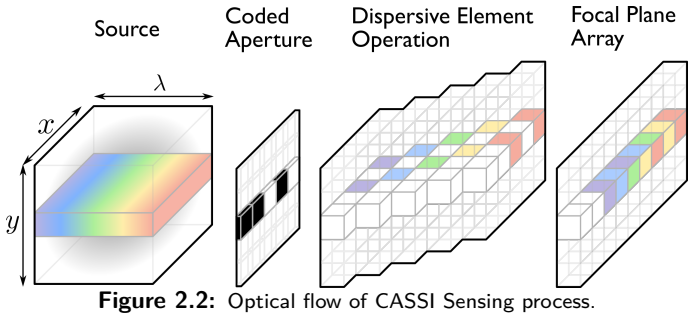


**Figure 2.2:** Optical flow of CASSI Sensing process.

### 2.1.1 Binary Coded Aperture (BCA)

In practice, the coded apertures are implemented through the use of digital micro-mirror devices (DMD) or photomasks. The distribution of the coded aperture entries can be optimized to achieve better reconstruction results, they can be generated completely at random to show the improvement of reconstruction. Furthermore, the use of random distributions entails high incoherence with the signal representation basis, which assures the correct reconstruction of the signal (Bernoulli distribution). Figure 2.3 shows an example of two typical coded aperture realizations with different transmittance levels, where the white pixels represent translucent elements that allow the light to pass through and the black pixels represent blocking elements.

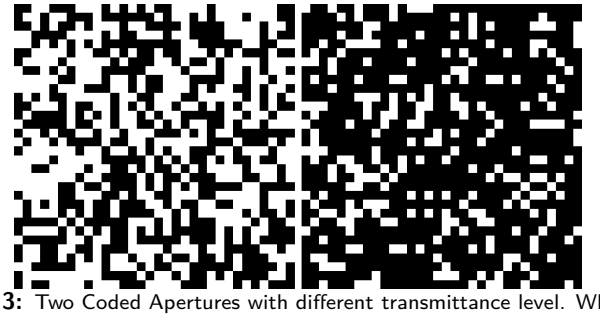

**Figure 2.3:** Two Coded Apertures with different transmittance level. White pixels allow the light to pass through, while black pixels block the light.

## 2.2 Colored Coded Apertures in CSI Systems

Traditional CSI systems use a set of Binary Coded Apertures (BCA), commonly realized through photomasks and digital micromirror device (DMD [24]), to modulate the spatial characteristics of the scene. This idea has been further extended by a group of CSI Systems that use Colored Coded Apertures (CCA) for spatial and spectral encoding [29, 30, 31].

Figure 2.4 illustrates the discretization process of three CSI systems based CCA, where each color in the CCA can be a low-pass, high-pass or band-pass for a fixed spectral range. In the first stage is located the Snapshot Colored Compressive Spectral Imager (SCCSI) proposed in [31], where the source is first dispersed by a dispersive element, encoded by an array of optical filters, and finally it is integrated in the spectral detector. In SCCSI, the nonlinear dispersion function of the prism is taken into account, however in this work the dispersion is assumed as a linear function in the discretization process [20]. Another CSI System is the Spatial-Spectral Encoded Compressive Spectral Imager (SSCSI) proposed in [32] which uses a single static coded mask in front of the sensor to achieve spatially non-uniform spectrum coding. However, as is shown in Figure 2.4, SSCSI can be expressed as spectral-spatial modulation by using CCA but without a dispersive element, where the spectral resolution is given by the number of color filters. In the last stage is the Colored Coded Aperture Spectral Imager (C-CASSI) proposed in [29]. In [30], the CCA are realizations of multiple 2D block-unblock coding (Spatial Coding) combined with multiple spectral filtering (Spectral Coding) as is showed in Figure 2.5. The Spatial Light Modulator can implemented by using a digital micromirror device (DMD) [24] and the spectral band filtering with Rotational Filter Wheel [33]. The 3D coding is finally registered in a 2D sensor intensity.

Let $\mathbf{F} \in \mathbb{R}^{N^2 \times L}$ that holding the structure

$$\mathbf{F} = \begin{bmatrix} f_{(1,1)} & \cdots & f_{(1,L)} \\ \vdots & \ddots & \vdots \\ f_{(N^2,1)} & \cdots & f_{(N^2,L)} \end{bmatrix} \tag{2.3}$$

with $N^2$ spectral vectors (the rows of $\mathbf{F}$), $L$ bands (the columns of $\mathbf{F}$) and $\mathbf{f} = \text{vec}(\mathbf{F})$. The CSI System can be written as the product of three matrices, each one representing an individual physical phenomenon for $\mathbf{f}$. The Figure 2.6 shows an example of C-CASSI System which can be expressed as

$$\mathbf{H}_{(k)} = \mathbf{PDC}_{(k)}, \ k = 1, ..., K, \tag{2.4}$$

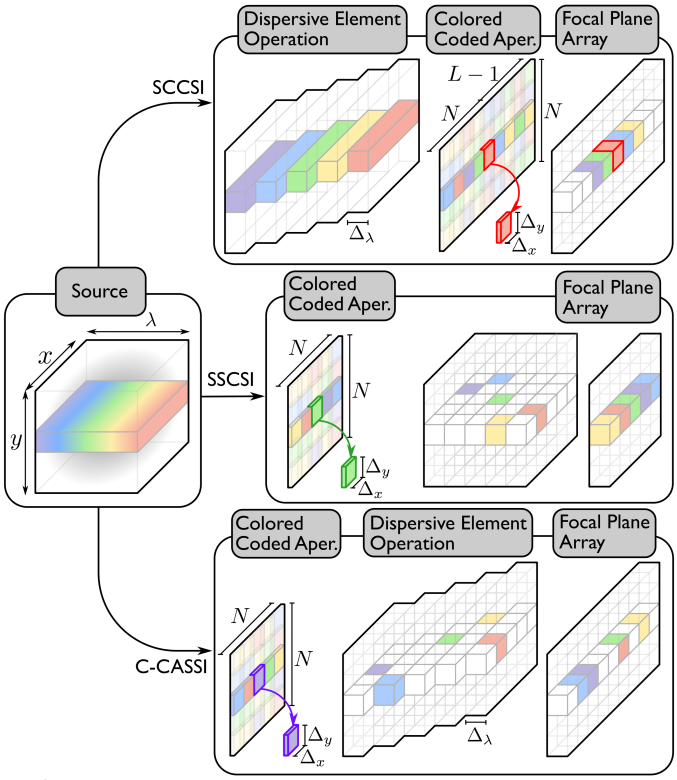


**Figure 2.4:** Illustration of the spatio-spectral optical flow for Snapshot Colored Compressive Spectral Imager (SCCSI) (top), Spatial-Spectral Encoded Compressive Spectral Imager (SSCSI) (middle) and Colored Coded Aperture Spectral Imager (C-CASSI) (bottom). Each square color in the Colored Coded Aperture is a spectral band filter.

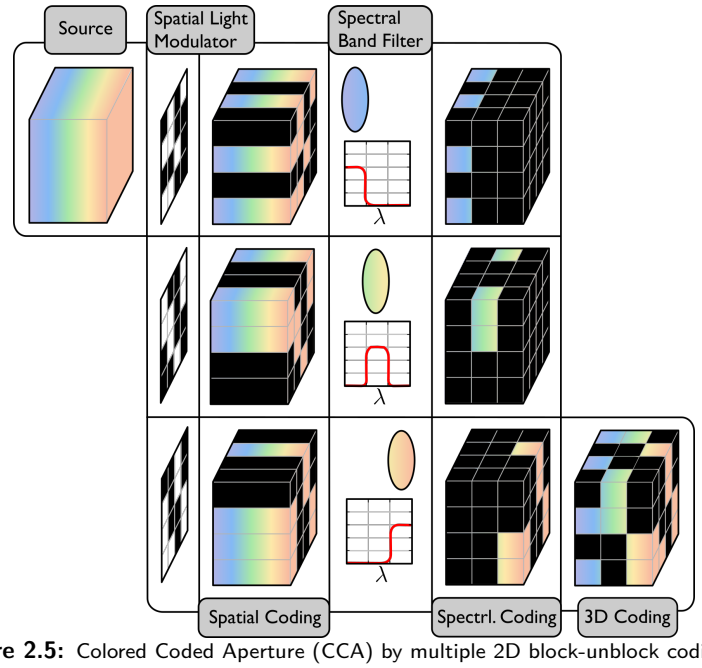


**Figure 2.5:** Colored Coded Aperture (CCA) by multiple 2D block-unblock coding for Spatial Coding and multiple spectral band filters for Spectral Coding.

where

- $\mathbf{H}_{(k)} \in \{0,1\}^{V \times N^2 L}$ is the $k$th projection with $V = N(N+L-1)$.
- $\mathbf{C}_{(k)} \in \{0,1\}^{N^2 L \times N^2 L}$ is the coding matrix, whose diagonal entries are the spectral responses of the CCA.
- $\mathbf{PD} \in \{0,1\}^{N(N+L-1) \times N^2 L}$ is the dispersion and integration phenomena.

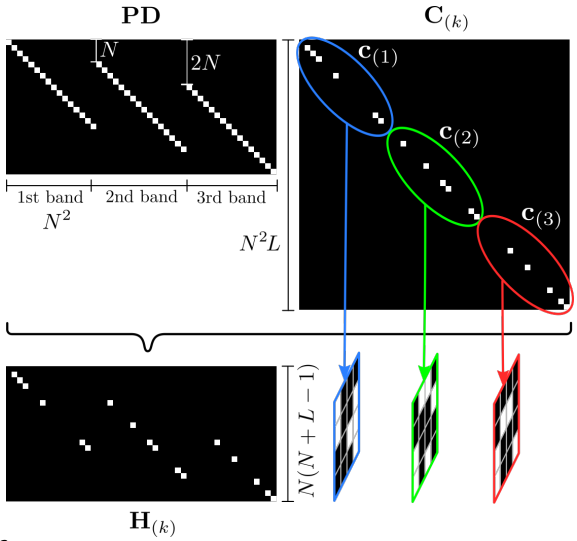


**Figure 2.6:** C-CASSI matrix $\mathbf{H}_{(k)}$ decomposed in $\mathbf{PD}$ and $\mathbf{c}_{(k)}$ are presented for $N = 4$, $L = 3$, and $V = N(N+L-1) = 24$. White squares represent a one-valued element (unblocking light). Each circle in the matrix $\mathbf{C}_{(1)}$ represents spatial modulation for each channel band.

The integration follows the structure $\mathbf{P} = \mathbf{1}^T \otimes \mathbf{I}_V$ where $\mathbf{1}^T$ is a one row vector with dimension $L$ and $\mathbf{I}_V$ is the identity matrix with dimension $V$. The dispersion matrix

$$\mathbf{D} = \begin{bmatrix} \mathbf{I}_{N^2} & \mathbf{0}_{T(L-1)\times N^2} & \cdots & \mathbf{0}_{T(1)\times N^2} \\ & \mathbf{I}_{N^2} & \ddots & \\ \mathbf{0}_{T(1)\times N^2} & \mathbf{0}_{T(2)\times N^2} & \cdots & \mathbf{I}_{N^2} \end{bmatrix} \tag{2.5}$$

where $T(l) = N(L-l)(N+L)$ and means the first size of zero matrix $\mathbf{0}$. On the other hand, for SSCSI, the dispersion effect is assumed as the identity matrix ($\mathbf{D} = \mathbf{I}_{N^2}$) and the integration matrix follows the structure $\mathbf{P} = \mathbf{1}^T \otimes \mathbf{I}_{N^2}$. In SSCSI, there is no overlapping between neighbourhood pixels (spectral signatures) due to the absence of the dispersion effect. In a more general way, the noise $K$ projection on $\mathbf{f}$ can be expressed as

$$\begin{bmatrix} \mathbf{y}_{(1)} \\ \vdots \\ \mathbf{y}_{(K)} \end{bmatrix} = \begin{bmatrix} \mathbf{H}_{(1)} \\ \vdots \\ \mathbf{H}_{(K)} \end{bmatrix} \mathbf{f} + \begin{bmatrix} \boldsymbol{\omega}_{(1)} \\ \vdots \\ \boldsymbol{\omega}_{(K)} \end{bmatrix} \tag{2.6}$$
$$\mathbf{y} = \mathbf{H}\mathbf{f} + \boldsymbol{\omega}$$

where $\boldsymbol{\omega}_{(k)} \in \mathbb{R}^{V \times 1}$ noise arises from a sampling process, $\mathbf{H} \in \{0,1\}^{KV \times N^2 L}$ is the concatenating of the $K$ projection of size $V$. Note that $\mathbf{H}$ leaves a sparse binary structure and the well condition of matrix $\mathbf{H}$ depends of the design of each $\mathbf{C}_{(k)}$, $k = 1, ..., K$. Starting from

$\mathbf{C}_{(k)} = \text{diag}([\mathbf{c}_{(1)}, ..., \mathbf{c}_{(L)}])$, where $\mathbf{c}_l \in \mathbb{R}^{N^2 \times 1}$, the spatial modulation $\mathbf{c}_l \sim$Bernoulli$(p)$, with probability $p$. The Figure 2.7 shows $\mathbf{c}_l$ for $l = 3$ and $p = 0.25$. The second row is a RGB representation of $([\mathbf{c}_{(1)}, \mathbf{c}_{(2)}, \mathbf{c}_{(3)}])$. This representation is the Colored Coded Aperture (CCA).

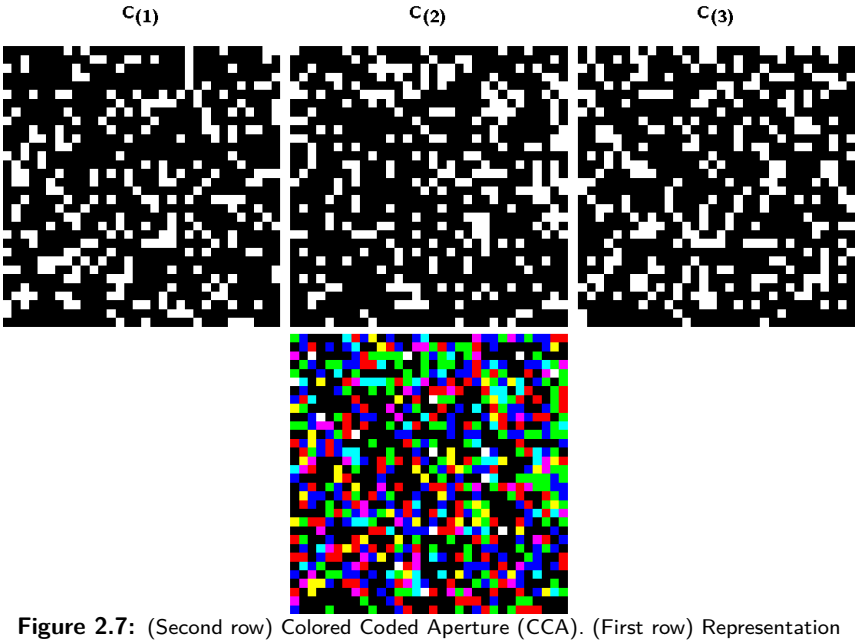


**Figure 2.7:** (Second row) Colored Coded Aperture (CCA). (First row) Representation of colored coded aperture by multiple BCA. Each $\mathbf{c}_{(l)}$ follow Bernoulli$(p)$ with $p = 0.25$.

In (2.6), each component $\boldsymbol{\omega}_{(k)}, k = 1, ..., K$ is Gaussian, $\boldsymbol{\omega}_{(k)} \sim \mathcal{N}(0, \sigma^2 \mathbf{I}_V)$ [8]. By taking the product of $K$ densities, the joint density $\boldsymbol{\omega} = [\boldsymbol{\omega}_{(1)}^T \cdots \boldsymbol{\omega}_{(K)}^T]^T$ is then $\boldsymbol{\omega} \sim \mathcal{N}(0, \sigma^2 \mathbf{I}_{KV})$, where $\mathbf{I}_{KV}$ is the identity matrix of dimension $KV$.

## 2.3 Compressive Sensing

CS exploits two main characteristics of spectral images:

- Due to the mixing phenomenon the spectral vectors belong to a low dimensional subspace.
- The data cube presents very high correlation in the spatial domain.

Then, the spectral data cubes are sparse and they admit a representation in a given basis or frame in which most of the coefficients are small and they are well approximated with a small number of large coefficients.

**Sparsity:** A signal $\mathbf{x}$ is $s$-sparse if it has at most $s$ nonzero entries. For example, for a 3-D signal $\mathbf{F} \in \mathbb{R}^{N \times N \times L}$ with $\mathbf{f} =$vec$(\mathbf{F})$ is said to be $s$-sparse, if there is a multidimensional basis $\overline{\boldsymbol{\Psi}}$ such that $\mathbf{x} = \overline{\boldsymbol{\Psi}}\mathbf{f}$ and only $s$ coefficients of $\mathbf{x}$ are nonzero with $s \ll N^2 L$ or

$$\mathbf{f} = \overline{\boldsymbol{\Psi}}_S^T \mathbf{x}_S \qquad S = \{n \in [N^2 L] : \mathbf{x}_n \neq 0\} \tag{2.7}$$

where $S$ is the index set of nonzero entries of $\mathbf{x}$. A multidimensional sparsifying basis is obtained using kronecker products as $\overline{\mathbf{\Psi}} = (\mathbf{\Psi}_1 \otimes \ldots \otimes \mathbf{\Psi}_D)$, where $D$ is the number of dimensions. Traditional basis functions are the wavelet transform, cosine transform, and pre-trained dictionaries [34, 35].

**CS Performance:** In order to define the problem in mathematical terms, let $\mathbf{f} \in \mathbb{R}^{N^2L}$ denote the CS measurements modeled as

$$\mathbf{y} = \mathbf{H}\mathbf{f} + \boldsymbol{\omega} = \mathbf{H}\overline{\mathbf{\Psi}}^T\mathbf{x} + \boldsymbol{\omega} \tag{2.8}$$

where the vector $\mathbf{y} \in \mathbb{R}^{KV}$ with $KV \ll N^2L$ containing the CS measurements contaminated by the measurement noise $\boldsymbol{\omega}$. One important goal of CS is to recover the signal $\mathbf{x}$ from the fewest possible measurements $\mathbf{y}$. Many vectors $\mathbf{x}$ can yield the measurements $\mathbf{y}$ due to the rank deficiency of matrix $\mathbf{A} = \mathbf{H}\overline{\mathbf{\Psi}}^T$. When the signal is sparse, it can be accurately recovered from its compressive measurements by solving the optimization problem

$$\min_{\mathbf{x}} \|\mathbf{x}\|_1 \text{ subject to } \|\mathbf{A}\mathbf{x} - \mathbf{y}\|_2^2 \leq \epsilon \tag{2.9}$$

where $\epsilon$ is an upper bound on the $\ell_2$ norm of the noise vector and $\|\cdot\|_1$ denotes the $\ell_1$ norm, which is equal to the sum of the absolute values of the vector entries. The restricted isometry property (RIP) has been proposed to measure the fitness of matrix $\mathbf{A}$. $s$-restricted isometry constant for the matrix $\mathbf{A}$, denoted by $\delta_s$ is the smallest nonnegative number such that, for all $\mathbf{x} \in \mathbb{R}^{N^2L}$ with $\|\mathbf{x}\|_0 = s$

$$(1 - \delta_s)\|\mathbf{x}\|_2^2 \leq \|\mathbf{A}\mathbf{x}\|_2^2 \leq \|\mathbf{x}\|_2^2(1 + \delta_s), \tag{2.10}$$

Equivalently, it is given by

$$\delta_s = \max_{S \subset [N^2L], \text{card}(S) \leq s} \|\mathbf{A}_S^T\mathbf{A}_S - \mathbf{I}\|_2^2 \tag{2.11}$$

Once the constant $\delta_s$ is determined, it can be used to guarantees for CS. Then, the matrix $\mathbf{A}$ satisfies the restricted isometry property if $\delta_s$ is small for reasonably large $s$. (2.10) applies when $\overline{\mathbf{\Psi}}$ is an orthonormal basis. Then, a good strategy for designing the $\mathbf{H}$ matrix is to draw the measurement explicitly from some orthonormal basis. For the choice of $\overline{\mathbf{\Psi}}$ and $\mathbf{H}$, the matrix $\mathbf{A}$ have efficient implementations (without requiring explicit matrix multiplications). This can help in developing fast algorithms for solving the reconstruction problem.

A critical condition for successful recovery of a sparse vector $\mathbf{x}$ depended on the properties of the product $\mathbf{H}\overline{\mathbf{\Psi}}^T$. This has been characterised using the properties of coherence and the RIP(2) [36]. The properties above hold for signals which are sparse in orthonormal basis, more specifically when $\overline{\mathbf{\Psi}}$ is orthonormal. However, there are signals that are expressed in terms of overcomplete dictionaries which are highly coherent. This makes difficult to ensure that $\mathbf{H}\overline{\mathbf{\Psi}}^T$ has low coherence (or satisfies the RIP(2)). Moreover, there is not a unique solution $\mathbf{x}$ from measurements $\mathbf{y}$ when $\overline{\mathbf{\Psi}}$ is highly coherent.

### 2.4 Optimal Colored Coded Aperture

Emerging research proposes to treat $\mathbf{H}$ and $\overline{\mathbf{\Psi}}$ separately when $\overline{\mathbf{\Psi}}$ is highly coherent [37]. With this, the matrix $\mathbf{H}$ has a small restricted isometry constant when a fewer subset of columns is approximately an orthonormal system. For a sparse and binary matrix the RIP($p$) property with $p = 1$ is satisfied with good sparse approximation recovery by a linear program when $\mathbf{H}$ has a constant column sum [38]. For the performance of the measurement basis, the correlation between distinct columns has been a fundamental index. The correlation between distinct columns of matrix $\mathbf{H}$ can be quantified as follows

$$\mu(\mathbf{H}) = \max_{1 \leq i,j \leq N^2 L, j \neq i} |\langle \mathbf{h}_{(i)}, \mathbf{h}_{(j)} \rangle| \tag{2.12}$$

The Mutual Coherence (MC) can be no larger than 1 when the columns of $\mathbf{H}$ have $\|\mathbf{h}_{(i)}\|_2 = 1$. Therefore, with the rough relation between the largest correlation and compressed sensing [39]

$$s < \frac{1}{2}(1 + 1/\mu(\mathbf{H})) \tag{2.13}$$

When $\mathbf{H}$ has a column constant sum $d$ the correlation values are taken from the set $1/d, ..., s/d$ and $\mu(\mathbf{H}) = (1/d)$ or $(s/d)$ [40]. From (2.9), for $\epsilon = 0$, if the system of linear equations $\mathbf{y} = \mathbf{H}\mathbf{x}$ has a solution satisfying $2s < \text{spark}(\mathbf{H})$, where $\text{spark}(\mathbf{H}) \leq \text{rank}(\mathbf{H}) + 1$ is the smallest number of linearly dependent columns of $\mathbf{H}$, it is necessarily the unique solution of (2.9) [39]. For $\epsilon > 0$, the concept of uniqueness of the sparsest solution is now replaced with the concept of stability [41]. From [41], $\mathbf{x}$ is unique and any solution $\mathbf{x}_\epsilon$ of (2.9) for a given $\epsilon > 0$ such that $\|\mathbf{y} - \mathbf{H}\mathbf{x}\|_2^2 \leq \epsilon$ satisfies

$$\|\mathbf{x} - \mathbf{x}_\epsilon\|_2 \leq \frac{4\epsilon^2}{1 - \mu(\mathbf{H})(2s - 1)} \tag{2.14}$$

Therefore, the MC plays an important role to guarantee exact signal recovery, and one would design $\mathbf{H}$ such that $\mu(\mathbf{H})$ is minimized. For instance, 2.8 depicts the case where a row of $\mathbf{H}$ has three unblocking elements. Bottom bar symbolizes the sum of the unblocking elements per column, having the same color convention as the right bar. Then a good measurement matrix satisfied

$$\begin{aligned} \mathbf{H} = (h_{(i,j)}): \quad & \sum_{i=1}^{KV} h_{(i,j)} = r \quad \text{for } i = 1, \ldots, N^2 L \\ & \sum_{j=1}^{N^2 L} h_{(i,j)} = c \quad \text{for } j = 1, \ldots, KV \\ & h_{(i,j)} \in \{0, 1\} \end{aligned} \tag{2.15}$$

where $h_{(i,j)}$ is the $\mathbf{H}$ element of the $i$th row and $j$th column with $\mathbf{H} \in \{0,1\}^{KV \times N^2 L}$. However, ensure that 2.15 is satisfied is very difficult when $\mathbf{H} \in \{0, 1\}$ and $KV < N^2 L$.

**Column and Row Homogenization:** It is possible to construct the coded aperture set from the system measurement $\mathbf{H}$ matrix based on two statistical parameters of $\mathbf{H}$, the average of unblocking elements per column ($M_y$) and the average of unblocking elements

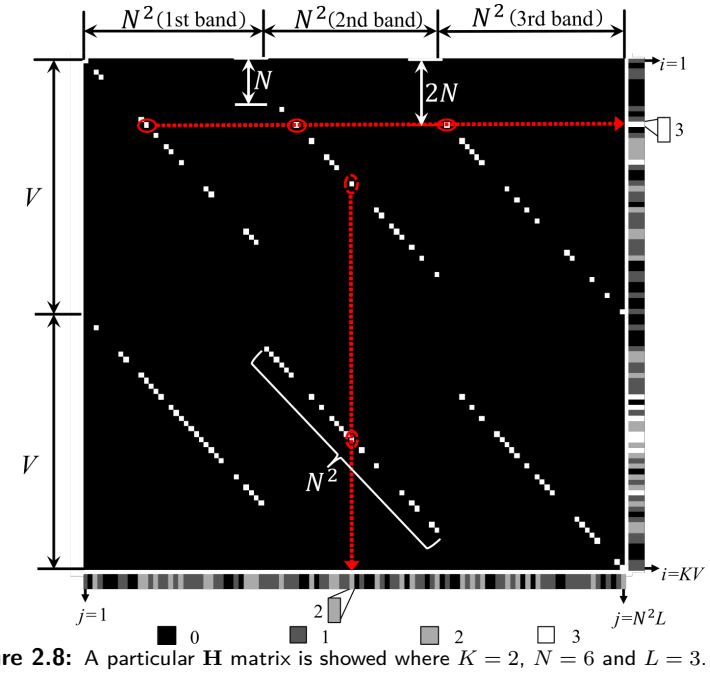


**Figure 2.8:** A particular $\mathbf{H}$ matrix is showed where $K = 2$, $N = 6$ and $L = 3$. White squares represent ones (un- blocking light element). Right bar represents the sum of the unblocking elements per row. Bottom bar represents the sum of the unblocking elements per column. Lower squares presents color convention for the bars.

per row ($M_x$). Let the average of unblocking elements per column and the average of unblocking elements per row defined as

$$\begin{aligned} M_y &= \sum_{j=1}^{N^2L} \frac{(\mathbf{c}_{(i)})}{N^2L} \quad \text{where } \mathbf{c}_{(i)} = \sum_{i=1}^{KV} h_{(i,j)} \ , i = 1, \ldots, KV \\ M_x &= \sum_{i=1}^{KV} \frac{(\mathbf{r}_{(j)})}{KV} \quad \text{where } \mathbf{r}_{(j)} = \sum_{j=1}^{N^2L} h_{(i,j)}, j = 1, \ldots, N^2L \end{aligned} \tag{2.16}$$

However, since $\mathbf{H}$ structure allows at most $K$ unblocking elements per row and L per column, $M_y$ and $M_x$ are not independent, in fact, they are related as

$$M_x = \frac{M_y L}{K} \tag{2.17}$$

Since $\mathbf{H}$ structure allows at most $K$ unblocking elements per row and $L$ per column, $M_y$ and $M_x$ are not independent, in fact, they are related as $M_x = M_y L/K$. Due to the prism effect is modeled in $\mathbf{H}$ by the shifting of the diagonals on each band there are three zones in the $\mathbf{H}$ matrix. The zones are defined according to the first shot. The $V$ rows are partitioned into the three zones as follows: since 1 to $N(L-1)$, since $N(L-1)+1$ to $N^2$ and since $N^2+1$ to $V$ for the first, second and third zone respectively. Figure 2.9 depicts the three zones for homogenization process. Taking into account the zones of $\mathbf{H}$, the problem is reduced to homogenize the submatrices $\mathbf{U}^i$ that vary in size with at most $K \times L$ dimension and $i = 1, \ldots, V$. Visually a $\mathbf{U}^i$ matrix is constructed taking $\mathbf{t}_k^l$ elements that are in same column and row of $\mathbf{H}$ according to the case. The matrices for $i = 11$ (case 1), 26 (case 2) and 45 (case 3), where it depicts how the row length of $\mathbf{U}^i$ changes in cases 1 and 3, but in case 2 it is constant having $L$ columns. The number of rows is

always $K$.

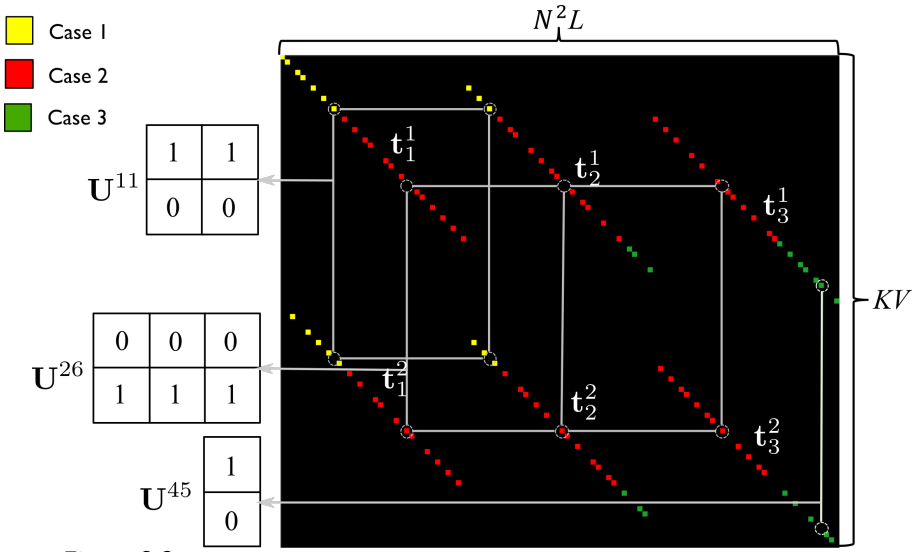


**Figure 2.9:** $\mathbf{H}$ matrix with $K = 2$, $N = 6$ and $L = 3$. The zones where each case takes place are illustrated, where yellow zone is for first case, red zone is for second case and green zone for third case.

Then, Homogenization receives as parameters $\mathbf{U}^i$, the number of shots $K$ and the amount of unblocking elements per column $M_y$ . It uses the relation in the 2.17 to find $M_x$ in rows of $\mathbf{U}^i$ once it has homogenized the columns. Nevertheless 2.17 outputs a rational number not always integer, for this reason, to reduce the standard deviation of the average of unblocking elements per row on every $\mathbf{U}^i$ matrix the algorithm recalculates $M_x$ as

$$M_x = \frac{M_y' Y}{K} \tag{2.18}$$

where $Y$ is the number of the columns of $\mathbf{U}^i$. Then, to guarantee the average does not change as it has been calculated in 2.17 it is necessary that some rows have an extra unblocking element. The number of rows that will have the extra element is calculated as:

$$P_x = M_y' Y - M_x K \tag{2.19}$$

The procedure of Algorithm 1 is as follows: If $S$ is negative, the function SetRandOnesCol randomly changes $\mid S \mid$ blocking elements for unblocking elements. On the contrary, if $S$ is positive the function SetRandOnesCol randomly removes $S$ unblocking elements turning them into blocking until there are $M_y'$ unblocking elements on the $j$th column. The function zeros creates a vector of zeros, and the function SetRandOnesColRow randomly selects an unblocking element on the $i$th row and turns it into a blocking element, then relocates that unblocking element randomly on the same column only being restricted by the rows where $S > 0$.

**Algorithm 1:** Homogenization

**Inizialization**: $\mathbf{U}$, $M'_y$, $K$

$Y = \text{columnsize}(\mathbf{U})$
**for** $j = 1$ to $Y$ **do**
  $\text{m} = \sum_{i=1}^{K} U_{(i,j)}$
  $S = M_y - \text{m}$
  $\mathbf{U} = \text{setRandOnesCol}(\mathbf{U}, j, S)$
**end for**
$M_x = \left\lceil \frac{M'_y Y}{K} \right\rceil$
$P_x = M'_y Y - M_x K$
$\mathbf{r} = \text{zeros}(K)$
$\mathbf{r} = \text{setRandOnesCol}(\mathbf{r}, 1, P_x)$
**for** $i = 1$ to $K$ **do**
  $\text{m} = \sum_{j=1}^{Y} U_{(i,j)}$
  $S = M_x + \mathbf{r}(i) - \text{m}$
  **if** $S < 0$ **then**
    **for** $k = 1$ to $\mid S \mid$ **do**
      $\mathbf{U} = \text{setRandOnesCol}(\mathbf{U}, i, M_x, \mathbf{r})$
    **end for**
  **end if**
**end for**

The Algorithm 1 returns a $\mathbf{U}^i$ matrix with $i = 1, \ldots, V$ where all its columns have the same number of unblocking elements and where the amount of unblocking element per row only differs between them with at best $\pm 1$. Finally, the homogenized $\mathbf{U}^i$ is reinserted in $\mathbf{H}$ by the main algorithm. Figure 2.10 shows the homogenization of the $\mathbf{H}$ matrix using Algorithm 1 with $M_y = 1$. Indeed, the uniform dark gray color in bottom bar indicates that $\mathbf{H}$ has been homogenized with one unblocking element per column.

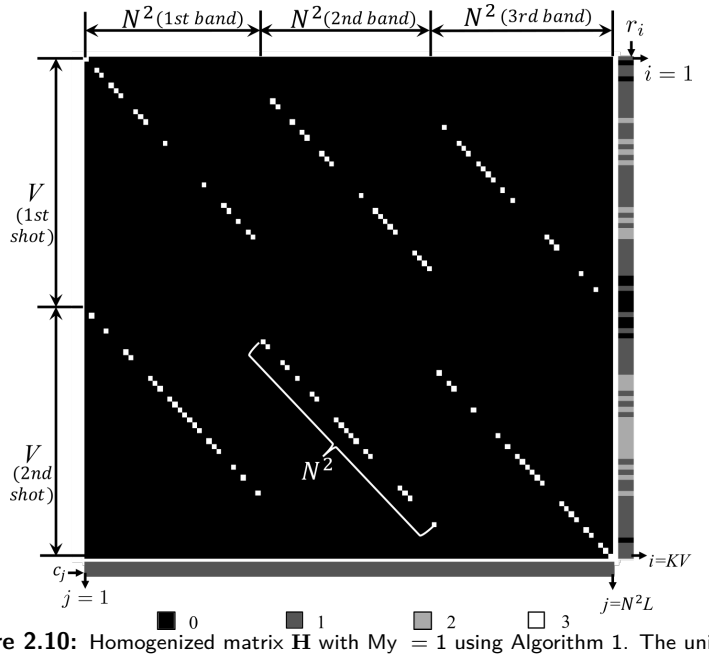


**Figure 2.10:** Homogenized matrix $\mathbf{H}$ with My $= 1$ using Algorithm 1. The uniform dark gray color in the bottom bar indicates that $\mathbf{H}$ has been homogenized with just one unblocking element per column.

**Resume CA:** The Figure 2.11 shows comparison example of three coded apertures. Note in Figure 2.11 that for CCA ($M_x = M_y = 1$), the sum of coded apertures only differs between them with at best $\pm 1$.

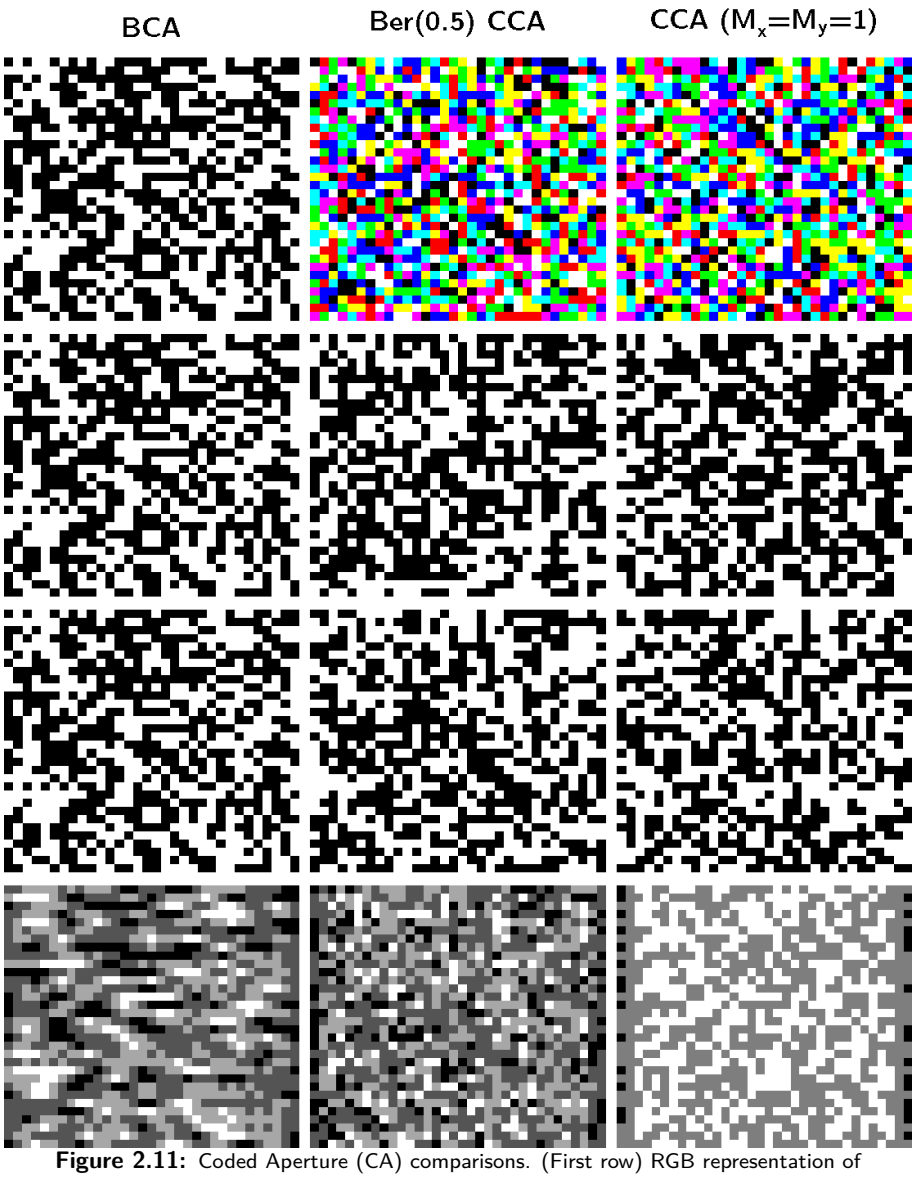


**Figure 2.11:** Coded Aperture (CA) comparisons. (First row) RGB representation of Binary Coded Aperture (BCA), Colored Coded Aperture (CCA) using Bernoulli distribution with $p = 0.5$, Homogenized Colored Coded Aperture with $M_x = M_y = 1$. (Second and Third row) Coded aperture in the first and second band. (Fourth row) Sum operation of three bands.

# 3

# Compressive Spectral Unmixing (CSU)

In this chapter, spectral unmixing concept and the use of CS can also assist with another important problem in spectral imaging that is the very large dimensionality of data sets. In CS the data is compressed in the acquisition process. In the case of remote sensing, the compressed data is then sent to earth. Later the compressed data is processed by taking advantage of the spectral image properties. This problem is attacked with a compressive unmixing model by assuming that the sparse basis vectors are the endmembers and the basis coefficient are the material abundances. Finally, an alternating optimization strategy is used to solve efficiently the new problem.

## 3.1 Problem Statement

Let $\{\mathbf{f}_{(n)}\}_{n=1,...,N^2}$ the set of spectral vectors of matrix $\mathbf{F}$ in (2.3). Each vector of set can be represented by a linear combination of basis vectors $\{\mathbf{m}_{(n_e)}\}_{n_e=1,...,N_e}$ as

$$\mathbf{f}_{(n)} = \sum_{n_e=1}^{N_e} a_{(n,n_e)}\mathbf{m}_{(n_e)}, \quad n = 1, ..., N^2 \tag{3.1}$$

where $a_{(n,n_e)}$ is the basis coefficient of $\mathbf{f}_{(n)}$ with respect to $\mathbf{m}_{(n_e)}$. According to the sparse linear mixing model (SLMM), described for instance in [42], assumes that the spectral scene, for a given pixel, is generated by a linear combination of a small number of deterministic spectral signatures known as endmembers. The basis vectors may be interpretable as the mixing matrix, holding the spectral signatures of the endmembers, and $a_{(n,n_e)}$ as the abundance coefficients of the spectral vector $\mathbf{f}_{(n)}$. Due to physical considerations, the abundance coefficients should satisfy two constraints the abundance non-negativity constraints (ANC) and the abundance sum-to-one constraints (ASC):

$$\begin{cases} a_{(n,n_e)} \geq 0, \quad n_e = 1, \dots N_e \\ \sum_{n_e=1}^{N_e} a_{(n,n_e)} = 1, \end{cases} \tag{3.2}$$

From (3.1), the matrix form of SLMM is given by

$$\begin{aligned}\begin{bmatrix}\mathbf{f}_{(1)}\\ \vdots \\ \mathbf{f}_{(N^2)}\end{bmatrix} &= \begin{bmatrix}a_{(1,1)} & \cdots & a_{(1,N_e)}\\ \vdots & \ddots & \vdots \\ a_{(N^2,1)} & \cdots & a_{(N^2,N_e)}\end{bmatrix}\begin{bmatrix}\mathbf{m}_{(1)}\\ \vdots \\ \mathbf{m}_{(N_e)}\end{bmatrix}\\ \mathbf{F} &= \mathbf{A}\mathbf{M},\end{aligned} \tag{3.3}$$

where $\mathbf{F}$ holds the structure of (2.3), $\mathbf{M} \in \mathbb{R}^{N_e \times L}$ is the sparse basis whose rows are the basis vectors and $\mathbf{A} \in \mathbb{R}^{N^2 \times N_e}$ is representation coefficients in a matrix form.

### 3.1.1 Compressive Model

After having the SLMM in (3.3), it is necessary to reformulate the representation into a CS framework. By using a tensor presentation [43] the SLMM is

$$\begin{aligned}\text{vec}(\mathbf{F}) &= (\mathbf{M}^T \otimes \mathbf{I}_{N^2})\text{vec}(\mathbf{A})\\ \mathbf{f} &= (\mathbf{M}^T \otimes \mathbf{I}_{N^2})\boldsymbol{a} = \overline{\mathbf{M}}\boldsymbol{a},\end{aligned} \tag{3.4}$$

where $\boldsymbol{a} \in \mathbb{R}^{N^2 N_e \times 1}$ is the collection of the abundance fractions for all the pixels in the scene and $\otimes$ is the Kronecker product operation on two matrices that combining a 1-D basis and 2-D to represent a 3-D given by

$$\mathbf{M}^T \otimes \mathbf{I}_{N^2} = \begin{pmatrix} m_{(1,1)}\mathbf{I}_{N^2} & \cdots & m_{(1,N_e)}\mathbf{I}_{N^2} \\ \vdots & \ddots & \vdots \\ m_{(L,1)}\mathbf{I}_{N^2} & \cdots & m_{(L,N_e)}\mathbf{I}_{N^2} \end{pmatrix} \tag{3.5}$$

Based on the tensor representation of the SLMM presented in (3.4), any linear projection applied to the left side of $\mathbf{f}$ describes a spectral and spatial modulation. Based on the advantages of te structure of the $\mathbf{H}$ matrix as the measurement basis is formulated the following representation for spectral unmixing based CS as

$$\begin{aligned}\mathbf{y} &= \mathbf{H}\mathbf{f} + \boldsymbol{\omega}\\ &= \mathbf{H}\overline{\mathbf{M}}\boldsymbol{a} + \boldsymbol{\omega},\end{aligned} \tag{3.6}$$

where (all dimension are summarized in Table 3.1)

- $\mathbf{y} \in \mathbb{R}^{KV \times 1}$ the compressive measurements.
- $\mathbf{H} \in \{0,1\}^{KV \times N^2 L}$ represents the spatial and spectral modulation.
- $\overline{\mathbf{M}} \in \mathbb{R}^{N^2 L \times N^2 N_e}$ is the 3-D basis.
- $\boldsymbol{\omega} \in \mathbb{R}^{KV \times 1}$ represents the additive noise random in the sampling process.

**Table 3.1:** Dimension summary.

| Variable | Description |
|---|---|
| $L$ | Number of spectral bands |
| $N$ | Spatial dimension of the data cube |
| $N_e$ | Number of endmembers |
| $K$ | Number of projections |
| $V$ | Size of each projection |

## 3.2 Problem Formulation

Bayesian estimation offers a solution to the inverse problem (3.6) that seeks the estimate $\boldsymbol{a}$ based on the relation between $\boldsymbol{a}$ and $\mathbf{y}$. The maximum likelihood (ML) estimation suggests finding the $\boldsymbol{a}$ that leads to the most probable set of measurements $\mathbf{y}$ as

$$\begin{aligned}\hat{\boldsymbol{a}}_{\mathrm{ML}} &= \max_{\boldsymbol{a}} \{p(\mathbf{y}|\boldsymbol{a})\} \\ &= \min_{\boldsymbol{a}} \left\{ \left(1/2\sigma^2\right) \|\mathbf{y} - \mathbf{H}\overline{\mathbf{M}}\boldsymbol{a}\|_2^2 \right\},\end{aligned} \tag{3.7}$$

There are several scenarios in which the ML estimates will be useful. However, for sparse estimation the ML demonstrates to be weak. A stabilized solution to the inverse problem (3.6) is the maximum a posteriori probability (MAP) estimator, which regularizes the estimation process using an assumed prior distribution on the signal.

### 3.2.1 MAP-Synthesis approach

The MAP is closely related to maximum likelihood (ML), but employs an augmented optimization objective which incorporates a prior distribution $p(\boldsymbol{a})$. A widely used sparseness prior for $p(\boldsymbol{a})$ is the Laplace prior. The Exponential prior is the positive version of the Laplace distribution which is known to be a good option for imposing sparsity on the solutions and is defined as

$$p(\boldsymbol{a}) = \lambda \prod_{n_e=1}^{N_e} \exp(-\lambda |a_{(n_e)}|) \text{ for } a_{(n_e)} \geq 0, \tag{3.8}$$

where $\lambda$ is the shape parameter of distribution. Merged with the Gaussianity assumption on the additive noise, the MAP recovery is

$$\begin{aligned}\hat{\boldsymbol{a}}_{\mathrm{MAP}} &= \max_{\boldsymbol{a}} \{p(\mathbf{y}|\boldsymbol{a})p(\boldsymbol{a})/p(\mathbf{y})\} \\ &= \min_{\boldsymbol{a}} \{-\log(p(\mathbf{y}|\boldsymbol{a})) - \log(p(\boldsymbol{a}))\} \\ &= \min_{\boldsymbol{a}\geq 0} \left\{ (1/2)\|\mathbf{y} - \mathbf{H}\overline{\mathbf{M}}\boldsymbol{a}\|_2^2 + \mu \sum_{n_e=1}^{N_e} |a_{(n_e)}| \right\},\end{aligned} \tag{3.9}$$

where $\mu = \lambda\sigma^2$ is a heuristically adapted regularization term, which controls the trade off between sparsity and reconstruction error. The penalty function is convex, guaranteeing a unique solution and an iterative algorithm is employed for the minimization of (3.9).

## 3.3 Optimisation scheme

The system $\mathbf{y} = \mathbf{H}\overline{\mathbf{M}}\boldsymbol{a}$ is underdetermined and the main idea is pushing the compression rate to the limits. The compressive unmixing algorithm estimates $\boldsymbol{a}$ by solving the convex optimization

$$\min_{\boldsymbol{a}\geq 0} \quad (1/2)\|\mathbf{y} - \mathbf{H}\overline{\mathbf{M}}\boldsymbol{a}\|_2^2 + \mu\|\boldsymbol{a}\|_1, \tag{3.10}$$

To solve the problem in (3.10), the large scale nonnegative $l_1$ version of [44] can be used. The method solves the problem in (3.10) using a preconditioned conjugate gradients (PCG)

to solve a newton system. However, for $\mathbf{y} = \mathbf{H}\overline{\mathbf{M}}\boldsymbol{a}$ many iterations of PCG are needed. The alternating direction method of multipliers (ADMM) is a better way to split (3.10) in subproblems [45, 46]. By choice of the new variables, the initial problem is converted into a sequence of much simpler problems. The ADMM version of (3.10) is

$$\begin{aligned} \min_{\boldsymbol{a},\mathbf{x}_1,\mathbf{x}_2} \quad & (1/2)\|\mathbf{y} - \mathbf{H}\mathbf{x}_1\|_2^2 + \mu\|\mathbf{x}_2\|_1 \\ \text{subject to} \quad & \overline{\mathbf{M}}\boldsymbol{a} = \mathbf{x}_1 \\ & \boldsymbol{a} = \mathbf{x}_2, \quad \mathbf{x}_2 \geq 0 \end{aligned} \tag{3.11}$$

the first term measures the estimation error and the second term promotes sparsity of abundance on dictionary. In compact form becomes [47]:

$$\begin{aligned} \min_{\boldsymbol{a},\mathbf{x}} \quad & g(\mathbf{x}) \\ \text{subject to} \quad & \mathbf{G}\boldsymbol{a} + \mathbf{B}\mathbf{x} = \mathbf{0} \end{aligned} \tag{3.12}$$

where

$$\begin{aligned} \mathbf{x} \quad &= (\mathbf{x}_1, \mathbf{x}_2) \\ g(\mathbf{x}) &= (1/2)\|\mathbf{y} - \mathbf{H}\mathbf{x}_1\|_2^2 + \mu\|\mathbf{x}_2\|_1 \end{aligned} \tag{3.13}$$

and

$$\mathbf{G} = \begin{bmatrix} \overline{\mathbf{M}} \\ \mathbf{I} \end{bmatrix} \quad \mathbf{B} = \begin{bmatrix} -\mathbf{I} & \mathbf{0} \\ \mathbf{0} & -\mathbf{I} \end{bmatrix} \tag{3.14}$$

the augmented Lagrangian for the problem is

$$\mathcal{L}(\boldsymbol{a}, \mathbf{x}, \mathbf{d}) = g(\mathbf{x}) + (\rho/2)\|\mathbf{G}\boldsymbol{a} + \mathbf{B}\mathbf{x} + \mathbf{d}\|_2^2 \tag{3.15}$$

with $\rho > 0$ as a positive constant. The ADMM algorithm for the formulation 3.12 is shown in Algorithm 2.

**Algorithm 2:** Alternating direction method of multipliers (ADMM) pseudocode

**Inizialization**: set $t = 0$, $\mu \geq 0$, $\boldsymbol{a}^{(0)}$, $\mathbf{x}^{(0)}$, $\mathbf{d}^{(0)}$

1: **repeat**
2: $\quad \boldsymbol{a}^{(t+1)} = \min_{\boldsymbol{a}} \mathcal{L}(\boldsymbol{a}^{(t)}, \mathbf{x}^{(t)}, \mathbf{d}^{(t)}, )$
3: $\quad \mathbf{x}^{(t+1)} = \min_{\mathbf{x}} \mathcal{L}(\boldsymbol{a}^{(t+1)}, \mathbf{x}^{(t)}, \mathbf{d}^{(t)})$
4: $\quad \mathbf{d}^{(t+1)} = \mathbf{d}^{(t)} + \mathbf{G}\boldsymbol{a}^{(t+1)} + \mathbf{B}\mathbf{x}^{(t+1)}$
5: **until**

### 3.3.1 Joint Sparsity

Due to the abundance maps exhibit piecewise smooth in the spatial domain [48] and they are scaled by a factor that is illumination variability [49] (the illumination variability can be estimated when the data cube is available). The joint sparsity version of (3.11) is

$$
\begin{aligned}
\min_{\boldsymbol{a},\mathbf{x}_1,\mathbf{x}_2,\mathbf{x}_3,\mathbf{x}_4} \quad & (1/2)\|\mathbf{y}-\mathbf{H}\mathbf{x}_1\|_2^2+\mu\|\mathbf{w}\circ\mathbf{x}_2\|_1+\mu_{\mathrm{TV}}\|\mathbf{x}_4\|_1 \\
\text{subject to} \quad & \overline{\mathbf{M}}\boldsymbol{a}=\mathbf{x}_1 \\
& \boldsymbol{a}=\mathbf{x}_2, \quad \mathbf{x}_2\geq 0 \\
& \boldsymbol{a}=\mathbf{x}_3 \\
& \mathbf{L}\mathbf{x}_3=\mathbf{x}_4
\end{aligned}
\tag{3.16}
$$

where $\mathbf{w}=\mathrm{diag}(w_{(1)},\ldots,w_{(N^2)})$ is a weighting vector, $\mathbf{L}=[\mathbf{L}_{\mathrm{h}};\mathbf{L}_{\mathrm{v}}]$ denotes the operator which computes the horizontal and vertical differences. The augmented Lagrangian of (3.16) is

$$
\begin{aligned}
\mathcal{L}(\boldsymbol{a},\mathbf{x}_1,\mathbf{x}_2,\mathbf{x}_3,\mathbf{x}_4,\mathbf{d}_1,\mathbf{d}_2,\mathbf{d}_3,\mathbf{d}_4)=(1/2)\|\mathbf{y}-\mathbf{H}\mathbf{x}_1\|_2^2+\mu\|\mathbf{w}\circ\mathbf{x}_2\|_1+\ldots \\
\mu_{\mathrm{TV}}\|\mathbf{x}_4\|_1+(\rho/2)\|\overline{\mathbf{M}}\boldsymbol{a}-\mathbf{x}_1+\mathbf{d}_1\|_2^2+(\rho/2)\|\boldsymbol{a}-\mathbf{x}_2+\mathbf{d}_2\|_2^2+\ldots \\
(\rho/2)\|\boldsymbol{a}-\mathbf{x}_3+\mathbf{d}_3\|_2^2+(\rho/2)\|\mathbf{L}\mathbf{x}_3-\mathbf{x}_4+\mathbf{d}_4\|_2^2
\end{aligned}
\tag{3.17}
$$

The pseudocode for Compressive Unmixing is shown in Algorithm 3. The term of the Step 4 in Algorithm 3 becomes, then

$$
\begin{aligned}
\boldsymbol{a}^{(t+1)}=\min_{\boldsymbol{a}} \quad & (\rho/2)\|\overline{\mathbf{M}}\boldsymbol{a}-\mathbf{x}_1+\mathbf{d}_1\|_2^2+(\rho/2)\|\boldsymbol{a}-\mathbf{x}_2+\mathbf{d}_2\|_2^2+\ldots \\
& (\rho/2)\|\boldsymbol{a}-\mathbf{x}_3+\mathbf{d}_3\|_2^2
\end{aligned}
\tag{3.18}
$$

The minimization of the augmented Lagrangian with respect to $\boldsymbol{a}$ is a quadratic problem

$$
\begin{aligned}
\boldsymbol{a}^{(t+1)}= \quad & (\overline{\mathbf{M}}^T\overline{\mathbf{M}}+2\mathbf{I}_{N^2N_e})^{-1}(\overline{\mathbf{M}}^T(\mathbf{x}_1^{(t)}-\mathbf{d}_1^{(t)})+(\mathbf{x}_2^{(t)}-\mathbf{d}_2^{(t)})+\ldots \\
& (\mathbf{x}_3^{(t)}-\mathbf{d}_3^{(t)}))
\end{aligned}
\tag{3.19}
$$

The minimization of the augmented Lagrangian with respect to $\boldsymbol{a}$ can be solved efficiently by the factor $(\overline{\mathbf{M}}^T\overline{\mathbf{M}}+2\mathbf{I}_{N^2N_e})^{-1}$ once, and then it uses this cached factorization in subsequent solve steps. The minimization with respect to $\mathbf{x}_2,\mathbf{x}_4$ is a component wise soft-threshold. The minimization with respect to $\mathbf{x}_1$ is a quadratic involving the inverse of the $(\mathbf{H}^T\mathbf{H}+\rho\mathbf{I}_{N^2L})^{-1}$ which, given the structure of the linear operator $\mathbf{H}$ is highly sparse, can be precomputed using the Cholesky factorization. Finally, the minimization with respect to $\mathbf{x}_3$ is also quadratic involving the inversion of $(\mathbf{L}^T\mathbf{L}+\mathbf{I}_{N^2N_e})^{-1}$ and it is is solved efficiently using Cholesky factorization [47].

**Algorithm 3:** Compressive Spectral Unmixing (CSU)

**Inizialization**: set $t = 0$, $\rho \geq 0$, $\mu \geq 0$, $\mu_{\text{TV}} \geq 0$, $\boldsymbol{a}^{(0)}$, $\mathbf{x}_1^{(0)}$, $\mathbf{x}_2^{(0)}$, $\mathbf{x}_3^{(0)}$, $\mathbf{x}_4^{(0)}$, $\mathbf{d}_1^{(0)}$, $\mathbf{d}_2^{(0)}$, $\mathbf{d}_3^{(0)}$, $\mathbf{d}_4^{(0)}$

**repeat**
  $\mathbf{w} = \text{diag}()$
  **for** $t = 1$ to MAXITER **do**
    $\boldsymbol{a}^{(t+1)} = \min_{\boldsymbol{a}} \mathcal{L}(\boldsymbol{a}^{(t)}, \mathbf{x}_1^{(t)}, \ldots, \mathbf{x}_4^{(t)}, \mathbf{d}_1^{(t)}, \ldots, \mathbf{d}_4^{(t)})$
    Update auxiliary variables
      $\mathbf{x}_1^{(t+1)} = (\mathbf{H}^T\mathbf{H} + \rho\mathbf{I}_{N^2L})^{-1}(\mathbf{H}^T\mathbf{y} + \rho(\overline{\mathbf{M}}\boldsymbol{a}^{(t+1)} + \mathbf{d}_1^{(t)}))$
      $\mathbf{x}_2^{(t+1)} = \max(0, \text{soft}(\boldsymbol{a}^{(t+1)} + \mathbf{d}_2^{(t)}, (\lambda/\rho)\mathbf{w}))$
      $\mathbf{x}_3^{(t+1)} = (\mathbf{L}^T\mathbf{L} + \mathbf{I}_{N^2N_e})^{-1}(\mathbf{L}^T(\mathbf{x}_4^{(t+1)} - \mathbf{d}_4^{(t)}) + (\boldsymbol{a}^{(t+1)} + \mathbf{d}_3^{(t)}))$
      $\mathbf{x}_4^{(t+1)} = \text{soft}(\boldsymbol{a}^{(t+1)} + \mathbf{d}_4^{(t)}, \mu_{\text{TV}}/\rho)$
    Update Lagrange multipliers
      $\mathbf{d}_1^{(t+1)} = \overline{\mathbf{M}}\boldsymbol{a}^{(t+1)} - \mathbf{x}_1^{(t+1)} + \mathbf{d}_1^{(t)}$
      $\mathbf{d}_2^{(t+1)} = \boldsymbol{a}^{(t+1)} - \mathbf{x}_2^{(t+1)} + \mathbf{d}_2^{(t)}$
      $\mathbf{d}_3^{(t+1)} = \boldsymbol{a}^{(t+1)} - \mathbf{x}_3^{(t+1)} + \mathbf{d}_3^{(t)}$
      $\mathbf{d}_4^{(t+1)} = \mathbf{L}\mathbf{x}_3^{(t+1)} - \mathbf{x}_4^{(t+1)} + \mathbf{d}_4^{(t)}$
  **end for**
**until**

# 4

# Simulations and Results

This section present numerical results on Compressive Spectral Unmixing (CSU) for supervised synthetic and semi-real data. The CSU scheme was implemented in a Matlab code and all numerical experiments were performed on a computer with Intel(R) Core(TM) i7-4790 CPU@3.60GHz and 32 GB RAM.

## 4.1 Evaluation metrics

Two metrics will be used to CSU scheme: the spectral angle distance (SAD) to dictionary prunning and the Signal-to-Reconstruction Error (SRE) to evaluate the quality of extracted fractional abundances.

**Spectral Angle Distance (SAD):** Some endmembers in the library are highly correlated and a pruning library technique is used. Pruning the spectral library reduce the complexity dramatically, and improve the unmixing results. The SAD between a reference signature $\mathbf{m}_{(i)}$ and an different spectral signature present in the dictionary $\mathbf{m}_{(j)}$ is given by the expression

$$\mathrm{SAD}(\mathbf{m}_{(i)}, \mathbf{m}_{(j)}) = \arccos\left(\frac{\langle \mathbf{m}_{(i)}, \mathbf{m}_{(j)} \rangle}{\|\mathbf{m}_{(i)}\| \|\mathbf{m}_{(j)}\|}\right) \tag{4.1}$$

**Signal-to-Reconstruction Error (SRE):** In order to analyze the quality of the unmixing results and evaluate the proposed method the reconstruction Signal-to-Reconstruction Error (SRE) is used and defined as

$$\mathrm{SRE} = 20\log_{10}\left(\frac{\|\boldsymbol{a}\|_2^2}{\|\boldsymbol{a} - \hat{\boldsymbol{a}}\|_2^2}\right) \tag{4.2}$$

where $\boldsymbol{a}$ is the vector containing the ground truth abundances, and $\hat{\boldsymbol{a}}$ is the vector containing the estimated abundances from compressed data. This error measure gives more information regarding the power of error in relation with the power of signal. An estimation of the abundance vector is considered successful if SRE(dB)= 5 dB or higher [42].

**Parameters in Algorithm 3:** By running a range of numerical experiments, heuristically, the vector of measurements $\mathbf{y}$ is scaled so that $\mathbf{y}_{\text{nrm}} = \mathbf{y}/\|\mathbf{y}\|_2$, and selected $\rho = 0.01$, $\mu = (1 \times 10^{-3})\|\mathbf{H}^T\mathbf{y}\|_\infty$, $\mu_{\text{TV}} = (1 \times 10^{-3})\|\mathbf{H}^T\mathbf{y}\|_\infty$. The maximum number of ADMM iterations has been fixed to 500 and the stopping rule is that the following condition is satisfied

$$\|\mathbf{r}^{(t+1)}\|_2 \leq (1 \times 10^{-4}) \quad \text{and} \quad \|\mathbf{s}^{(t+1)}\|_2 \leq (1 \times 10^{-4})$$

where $\mathbf{r}^{(t+1)} = \mathbf{G}\boldsymbol{a}^{(t+1)} + \mathbf{B}\mathbf{x}^{(t+1)}$ is the primal residual and $\mathbf{s}^{(t+1)} = \rho\mathbf{G}^T\mathbf{B}(\mathbf{x}^{(t+1)} - \mathbf{x}^{(t)})$ is the dual residual [47].

### 4.2 Spectral data used in the experiments

The contributions of this thesis are the development of a framework of CSU based on optimal CCA and testing a set of experimental data, in this way realizing a comparison between different approaches based CA. Multiple experiments are carried out with synthetic and real spectral datasets. The reason for the use of synthetic dataset is that all details of the simulated images are known and the algorithm performance can be examined in a controlled manner.

#### 4.2.1 Synthetic data

To verify the performance of proposed method, two experiments are carried out. The endmember data set was generated using real signatures from United States Geological Survey (USGS) digital spectral library [1]. The abundances are generated with the *Hyperspectral imagery Synthetisis toolbox for MATLAB* available online [2].

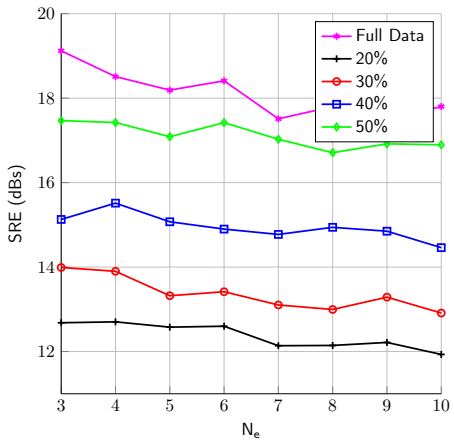


**Figure 4.1:** Plot of the SRE(dB) values (as a function of the number of endmembers) obtained by different compression levels when applied to the simulated data with noise 30 dB (SNR).

**Experiment 1:** The main goal of this experiment is to analyze the performance of CSU scheme when a spectral library is available apriori by enforcing the sparsity of the solution. The fractional abundances were randomly generated with Hyperspectral imagery

[1] http://speclab.cr.usgs.gov/spectral.lib06

[2] http://www.ehu.eus/ccwintco/index.php/Hyperspectral_Imagery_Synthesis_tools_for_MATLAB

Synthetisis toolbox of dimension $64 \times 64$. The mixtures are affected by noise ($\boldsymbol{\omega} \neq 0$) set to 30 dBs. For each compression level spectral library, it was generated 100 mixtures containing random endmembers from the library. From USGS, a pruned version was obtained by simply removing some of the spectral signatures which form a spectral angle smaller than $10°$. To reduce the computational complexity, the signatures are re-sampled and the number of bands $L = 64$ from 383 to 2508 $nm$. The Algorithms 3 have been applied to unmix simulated mixtures containing a number of endmembers $N_e$, which ranges from 3 to 10. 50 Monte Carlo simulations have been implemented and all the results have been obtained by averaging these 50 Monte Carlo runs.

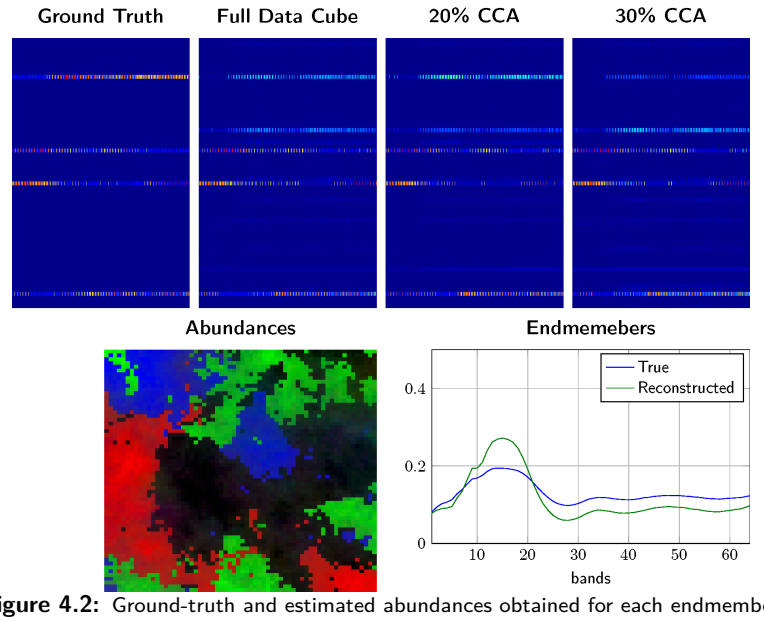


**Figure 4.2:** Ground-truth and estimated abundances obtained for each endmember material in the spectral library in affected by noise of 30 dBs. (Blue) True and (green) reconstructed spectra from a spectral library without pruning.

Figure 4.1 shows the SRE (dBs) values as a function of the number of endmemeber for different compression ratios (SNR of 30 dBs). Note that to low % of measures the curves of SRE show poor unmixing. However, even in 20% of measures using CCA with $M_x = M_y = 1$, the sparse abundances archived the minumum SRE (dBs) [42]. Also, the Sparse recovery exhibit not only a better performance when the number of endmembers is low, but also higher cardinalities when there are noise. This is because the endmembers in each synthetic experiment are randomly selected from spectral library pruned which means that they are easy to identify. By contrast, if spectral library are not pruned, the endmembers will be difficult to distinguish. For illustrate this, Figure 4.2 shows estimated abundances obtained from a not pruned spectral library and noise 30 dBs. Observe that in each estimated abundances there are more extra lines compared from ground Truth (The extra endmember estimated is plotted in the Figure 4.2). This is because in the spectral library is highly correlated, then is very difficult to identify real endmemebers. To concluded that not only the compression rate affect endmember estimation, but also the highly correlated spectral libray.

**Experiment 2:** In this experiment, the compressive spectral unmixing from (3.6) by using different CSI systems and fixed $\mathbf{M}$ is considered. The performances of the considered CSU scheme is evaluated with different compression levels. The simulated spectral sig-

natures are shown in Figure 4.3. Each experiment is repeated 20 times and their mean is reported. To reduce the computational complexity, the signatures are re-sampled and the number of bands $L = 128$ from 383 to 2508 $nm$. The number of endmembers is fixed to $N_e = 4$ and $\mathbf{A} \in \mathbb{R}^{N^2 \times N_e}$ with $N = 128$. The fractional abundances satisfy the ANC, ASC and are piecewise smooth as is shown in Figure 4.3. The synthetic data is then generated by the product of endmembers and abundances. Later, the data is projected on $\mathbf{H}$ using different compression levels. Specifically, are used Bernoulli$\sim$ (0.5) BCA [20], Bernoulli$\sim$ (0.5) CCA [30, 31], and Homogenised CCA for column ($M_x$) and row ($M_y$) mean equal to $1, 2, 3$. Zero-mean Gaussian noise is added to the synthetic data (20 dBs ).

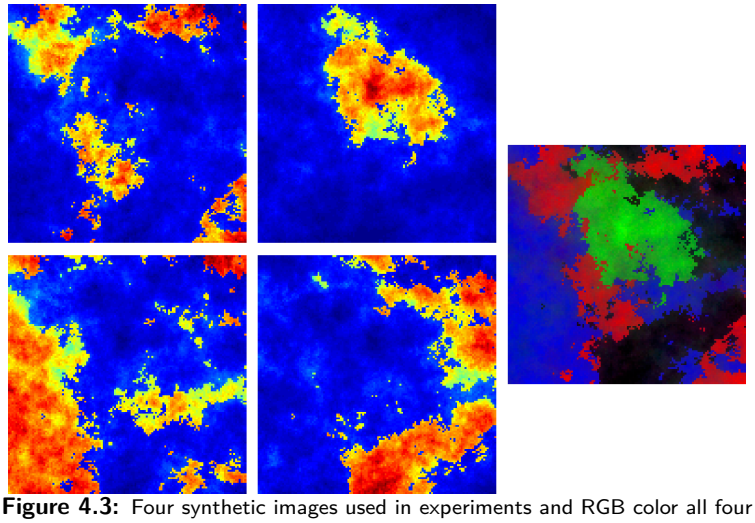

**Figure 4.3:** Four synthetic images used in experiments and RGB color all four abundance maps. Synthetic images are piecewise smooth.

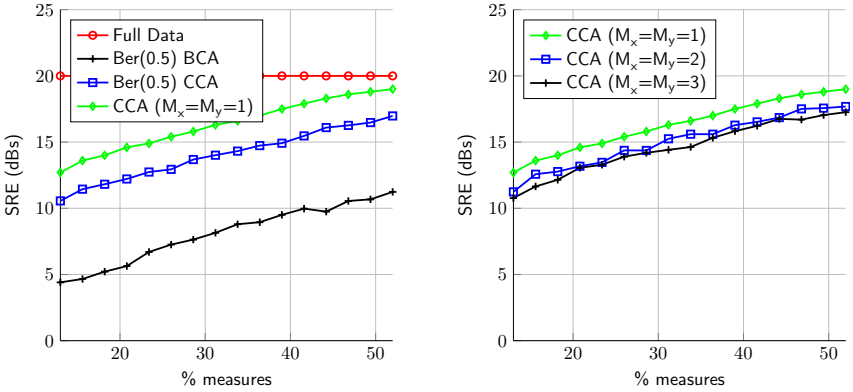


**Figure 4.4:** Plot of the SRE(dB) values (as a function of the % measures) obtained by Algorithm 3 and different CA when applied to the simulated data with zero-mean Gaussian noise (SNR = 20 dB).

Numerical results of the SRE (dB) is shown in Figure 4.4. For the proposed CSU the synthetic data and Algorithm 3 are used. Figure 4.4 also presents the results achieved using different CA applied on the synthetic data cube with different compression levels. Note in Figure 4.4 that almost all the CCA are able to recover the fractional abundances with adequate accuracy. Bernoulli codes also recover the fractional abundances with less accuracy and higher number of measurements are required for better estimation of the fractional abundances. Note also in Figure 4.4 that an improvement in the accuracy of more than

3 dB is achieved by the Homogenised CCA in comparison with the Bernoulli CCA. This improvement is due to the fact that Homogenised CCA leaves less correlation on $\mathbf{H}$. From (Figure 4.4), the performance of the homogenised CCA is maximum when $M_x = M_y = 1$ and becomes similar when $M_x = M_y = 2$ and $M_x = M_y = 3$ when the noise level is 20 dBs.

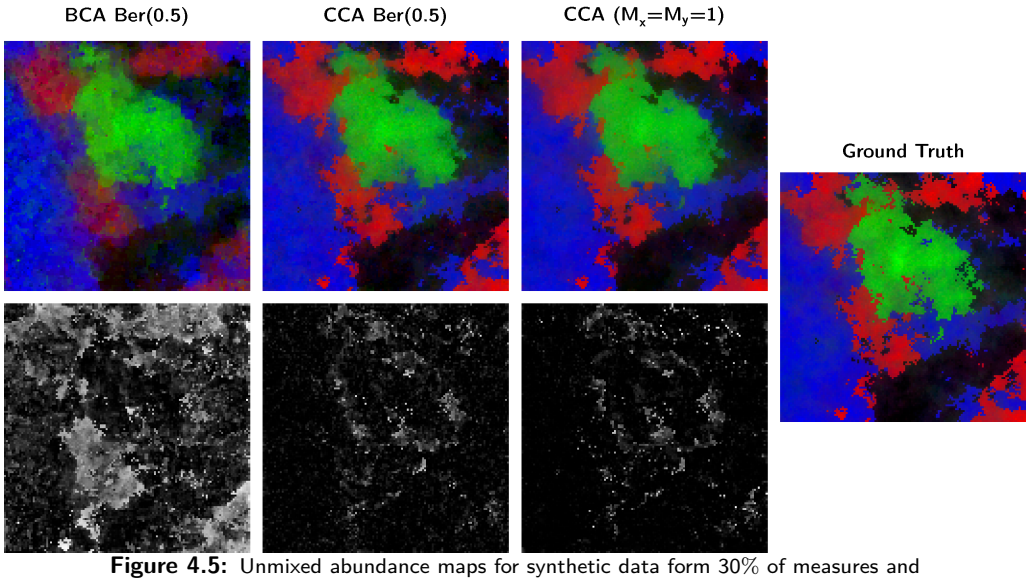


**Figure 4.5:** Unmixed abundance maps for synthetic data form 30% of measures and noise 30 SNR. Estimated abundance maps using (Row 1). Error map with respect the Ground Truth (Row 2).

For illustrative purposes, error maps is shown in Figure 4.5. In the first row the estimated abundance are obtained from 30% compressive measurements using the Algorithm 3 and different CA codes. In the second row of Figure 4.5 shows each error map with respect the Ground Truth. Visually, the Homogenised and Berboulli CCA offer much smaller error. Note also, that the abundance planes obtained with Bernoulli codes are estimated with higher error.

### 4.2.2 Real data

In addition to synthetic data experiments, it is very important to measure CSU performance using real data sets. In this section, the proposed CSU scheme is evaluated in real datasets, for which the real spectral image is the reference image and the compresive spectral image is realized from the reference image with additive noise.

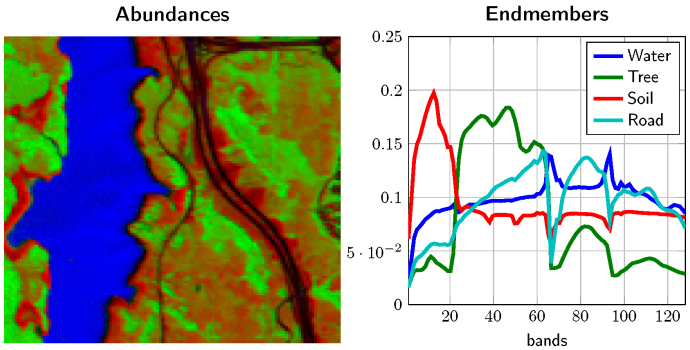


**Figure 4.6:** Jasper Ridge and its ground truth.

**Jasper Spectral Image:** Jasper Ridge is a popular spectral data used for unmixing experiments. There are $512 \times 614$ pixels in it. Each pixel is recorded at 224 channels ranging from $380nm$ to $2500nm$. The spectral resolution is up to $9.46nm$. Since this spectral image is too complex to get the ground truth, we consider a subimage of $128 \times 128$ pixels. The first pixel starts from the (105,269)-th pixel in the original image. By removing the channels 1–3, 108–112, 154–166 and 220–224 (due to dense water vapor and atmospheric effects) remaining 198 channels. Later, spectral bands are resampled to 128 channels. There are four endmembers latent in this data: Road, Soil, Water and Tree.

| Column and row mean $(M_y, M_x)$ | 40% | 30% | 20% |
|---|---|---|---|
| 1 | 12.42 | 11.85 | 10.09 |
| 2 | 11.71 | 10.99 | 9.07 |
| 3 | 10.23 | 9.71 | 8.88 |

**Table 4.1:** SRE (dBs) for Jasper abundance map from different compression ratios and Homogenized versions of $\mathbf{H}$ matrix (with noise 30 dBs).

The goal of this experiment is to analyze the performance of CSU on Jasper Ride data set from different compression rates. Due to the best performance obtained in the CSU experiments was when the CCA are optimized with parameters $M_x = M_y = 1, 2, 3$. Then, Jasper Ride scene has also considered with the same parameter cases as in the experiment with simulated data and different compression ratios. However, in this case the mixing matrix was estimated from the original data using the VCA [49]. The number of endmembers to be extracted was set to $N_e = 4$ in all experiments. After that, 30 dBs of additive noise was added for simulating model error and system noise. That noise was chosen by multiple experiments with VCA algorithm with real data.

The Table 4.1 shows the abundance maps estimated from 40%, 30% and 20% over 20 Monte-Carlo runs for the proposed method (Algorithm 3) with different compression ratios over the Jasper Ridge and each version of Homogenized matrix $\mathbf{H}$ ($M_x = M_y = 1, 2, 3$). It can be noticed that qualitatively there is a small difference between each sampling ratios schemes. Note also that quantitatively SRE in each sampling ratios is near to 10 (this implies good quality abundance map recovery). Slightly worse performance in the three ($M_x = M_y = 3$) case which is probably due to the fact that the endmember are estimating from more correlated version of $\mathbf{H}$. For illustrative purposes, Figure 4.7 shows the original abundances map and different compression ratios for the CSU algorithm. The first row is the RGB version of four abundances maps, the second to fifth row are individual abundance map (road, water, soil and three). The columns represent different error maps from different compression ratios. In this figure, it can see that, even in the worst case, the abundances estimation preserves the shape of the original, which means that the features of the signature are preserved. Furthermore, Figure 4.7 indicates that most of the pixels have a very low estimation error, which means that the estimated and the original abundances are very similar in most of the cases. This proves the effectiveness of the proposed CSU framework using joint sparsity information.

**Urban Spectral Image:** Urban is one of the most widely used spectral data used in the spectral unmixing study. There are $307 \times 307$ pixels and 210 wavelengths ranging from $400nm$ to $2500nm$, resulting in a spectral resolution of 10 nm. After the channels 1–4,

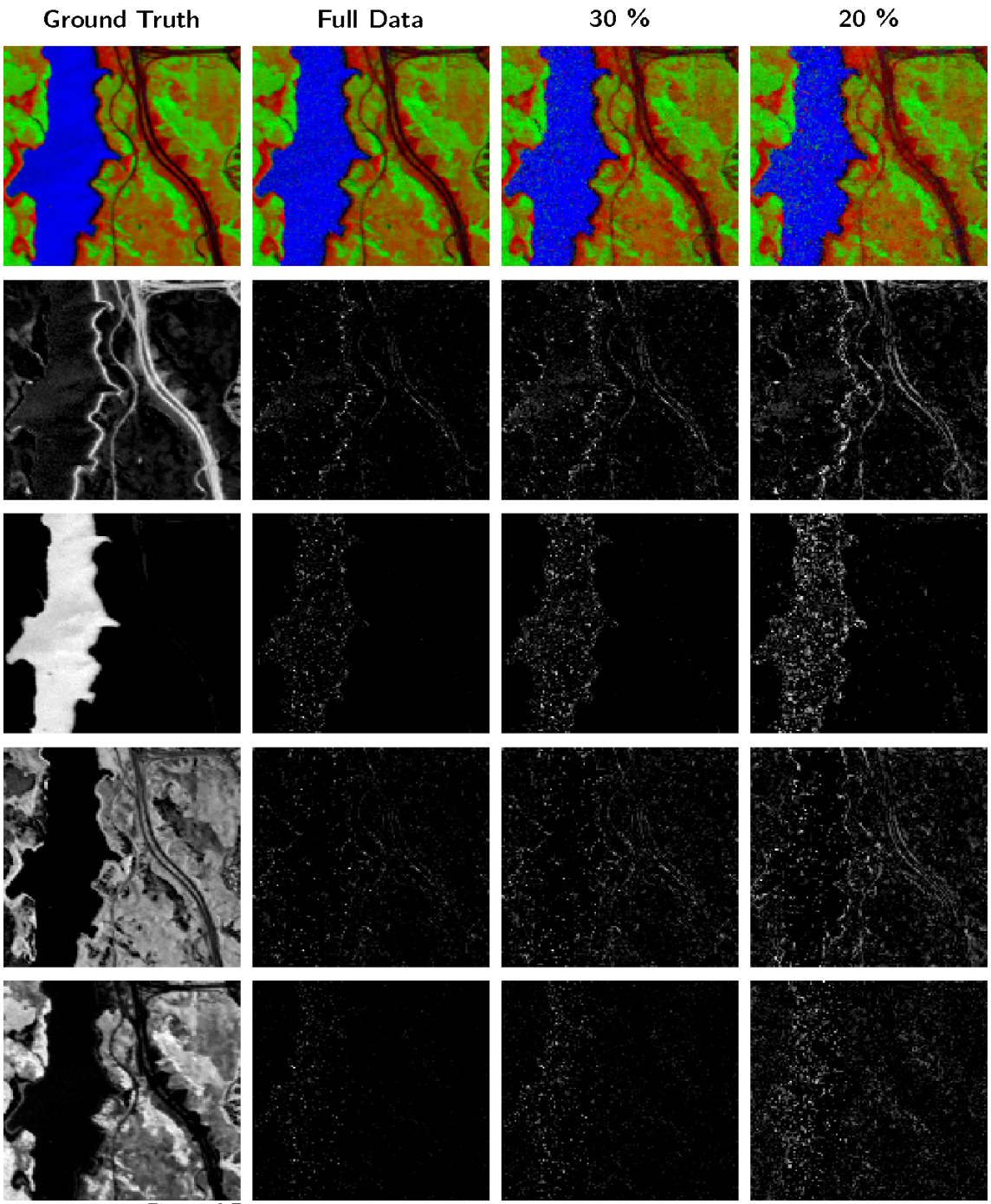


**Figure 4.7:** Error map between the original and the estimated abundance map form Jasper Ridge dataset for different compression ratios. Each row of the figure is a diferent abundance material (road, water, soil and three).

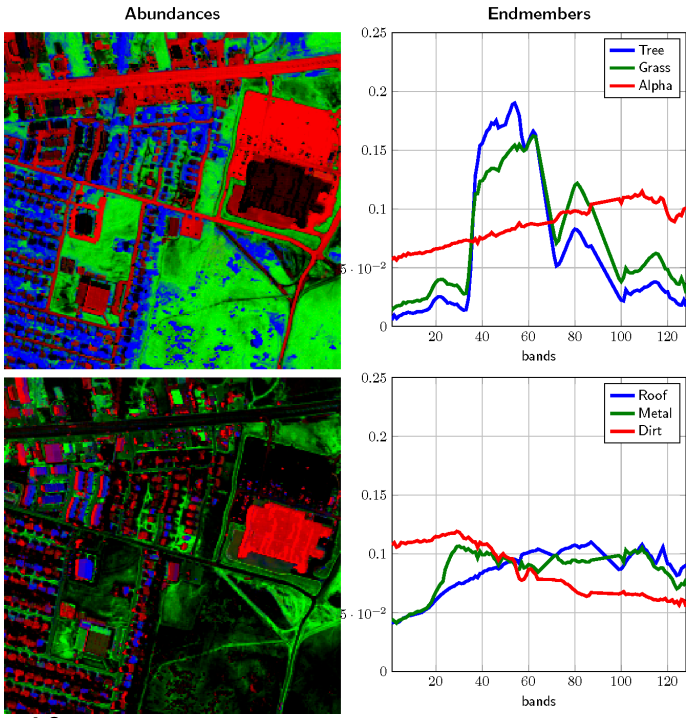


**Figure 4.8:** Urban spectral database and its ground truth (6 endmember version).

76, 87, 101–111, 136–153 and 198–210 are removed (due to dense water vapor and atmospheric effects), remaining 162 channels. To reduce the computational complexity, the signatures are resampled so the number of bands is 128 and the $256 \times 256$ pixels. The spectral signatures are shown in Figure 4.8.

| $\mu_{\text{TV}}$ | 40% | 30% | 20% |
|---|---|---|---|
| 0.005 | 10.42 | 9.8 | 8.46 |
| 0.001 | 11.71 | 11.12 | 9.92 |
| 0.0001 | 10.31 | 9.23 | 8.03 |

**Table 4.2:** SRE(dB) with diferent parameters $\mu_{\text{TV}}$ for Urban and compression ratios (noise 30 dBs).

The performance of the proposed joint regularizer using the real data cubes Urban. The algorithms were tested using different values of the parameters $\mu_{\text{TV}} = 0.005, 0.001, 0.0001$. All possible combinations of these parameters were considered. Table 4.2 shows the SRE(dB) results achieved by the different compression rations with the considered real data sets, using all considered SNR levels. Note that the inclusion of a second regularizer offers the potential to improve unmixing performance. Due to the fact that, with low noise conditions the l2 −l1 norm optimization solution are able to recover the fractional abundances with good accuracy. However, as the % of measures increase, the spatial term becomes more important and improves significantly the quality of unmixing results as it can be observed in the Figure 4.9.

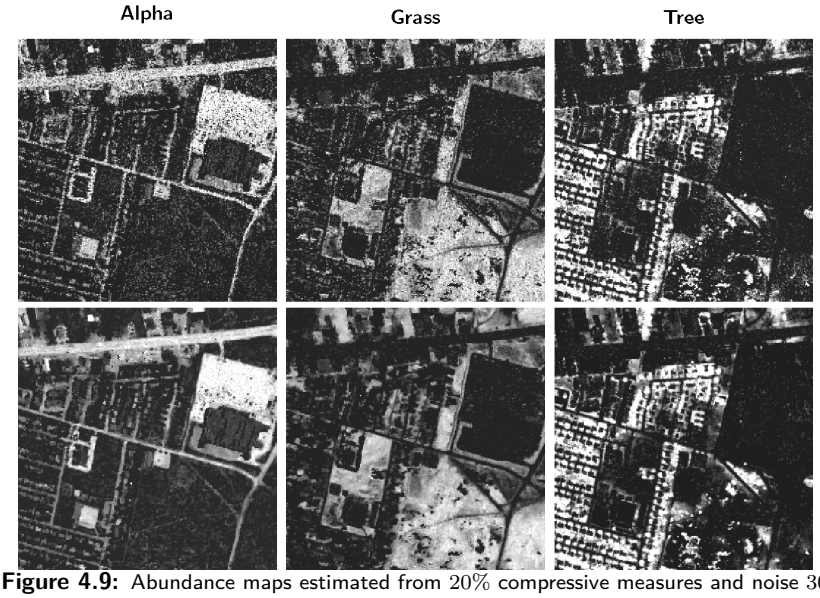


**Figure 4.9:** Abundance maps estimated from $20\%$ compressive measures and noise $30$ dBs. (First row) $\mu_{\mathsf{TV}} = 0.0001$ and (Second row) $\mu_{\mathsf{TV}} = 0.001$.

# 5

# Conclusions

In this work, a linear mixture model into compressive spectral imaging system has been used, which find the unmixed set of abundance maps from a set of compressive measures. The proposed scheme exploits that every spectral pixel is sparse in known spectral library of endmembers. The sparse vector is recovered solving a sparse nonnegative least square problem based augmented direction method of multiplier.

This thesis address the problem mentioned above and contributed an innovative scheme that provide the solution to the specific problem. The proposed scheme is based in CCA and allows unmixing from projected data cubes, having larger regions with mixed data than could be restored by preprocessing methods unaware of the signal subspace. The CSU scheme not require forming or storing any full-size data cube and consists of three major steps: Data acquisition by CS and data unmixing by solving a compressed unmixing model with spatial regularization on abundance fractions.

In this first-stage the CCA are study with respect a set of spectral signatures of the endmembers that are approximately known. The CCA are optimized using heuristically algorithm and projected on data cube. The data size to be processed becomes much smaller and independent of the number of spectral bands. An efficient algorithm has been constructed for solving a compressed unmixing model based on the augmented Lagrangian method and alternating minimization. The proposed CSU scheme has been empirically validated using both synthetic data and semi-real data. The impact of spatial information has been evaluated for endmember detection and abundance estimation. Numerical results clearly demonstrate that compressively acquired data of size ranging from 10% to 25% of the full size can produce satisfactory results. The results show some advantages of the inclusion of spatial information, in particular, when the noise level in the hyperspectral data is relatively high. These advantages are particularly apparent with the real spectral data considered in experiments.

# Bibliography


[1] R. O. Green, M. L. Eastwood, C. M. Sarture, T. G. Chrien, M. Aronsson, B. J. Chippendale, J. A. Faust, B. E. Pavri, C. J. Chovit, M. Solis, *et al.*, "Imaging spectroscopy and the airborne visible/infrared imaging spectrometer (aviris)," *Remote Sensing of Environment*, vol. 65, no. 3, pp. 227–248, 1998.

[2] N. Gat, "Imaging spectroscopy using tunable filters: a review," in *AeroSense 2000*, pp. 50–64, International Society for Optics and Photonics, 2000.

[3] N. Keshava, "A survey of spectral unmixing algorithms," *Lincoln Laboratory Journal*, vol. 14, no. 1, pp. 55–78, 2003.

[4] A. Wagadarikar, R. John, R. Willett, and D. Brady, "Single disperser design for coded aperture snapshot spectral imaging," *Applied optics*, vol. 47, no. 10, pp. B44–B51, 2008.

[5] Y. Guan, S. Guo, Y. Xue, J. Liu, and X. Zhang, "Application of airborne hyperspectral data for precise agriculture," in *Geoscience and Remote Sensing Symposium, 2004. IGARSS'04. Proceedings. 2004 IEEE International*, vol. 6, pp. 4195–4198, Ieee, 2004.

[6] W. L. Smith, D. K. Zhou, F. W. Harrison, H. E. Revercomb, A. M. Larar, H.-L. Huang, and B. Huang, "Hyperspectral remote sensing of atmospheric profiles from satellites and aircraft," in *Second International Asia-Pacific Symposium on Remote Sensing of the Atmosphere, Environment, and Space*, pp. 94–102, International Society for Optics and Photonics, 2001.

[7] M. Gehm, M. Kim, C. Fernandez, and D. Brady, "High-throughput, multiplexed pushbroom hyperspectral microscopy," *Optics express*, vol. 16, no. 15, pp. 11032–11043, 2008.

[8] D. J. Brady, *Optical imaging and spectroscopy*. John Wiley & Sons, 2009.

[9] A. Plaza, J. A. Benediktsson, J. W. Boardman, J. Brazile, L. Bruzzone, G. Camps-Valls, J. Chanussot, M. Fauvel, P. Gamba, A. Gualtieri, *et al.*, "Recent advances in techniques for hyperspectral image processing," *Remote sensing of environment*, vol. 113, pp. S110–S122, 2009.

[10] M. J. Golay, "Multi-slit spectrometry," *JOSA*, vol. 39, no. 6, pp. 437–444, 1949.

[11] M. Breuer and J. Albertz, "Geometric correction of airborne whiskbroom scanner imagery using hybrid auxiliary data," *International Archives of Photogrammetry and Remote Sensing*, vol. 33, no. B3/1; PART 3, pp. 93–100, 2000.

[12] N. Keshava and J. F. Mustard, "Spectral unmixing," *IEEE signal processing magazine*, vol. 19, no. 1, pp. 44–57, 2002.

[13] M. Parente and A. Plaza, "Survey of geometric and statistical unmixing algorithms for hyperspectral images," in *2010 2nd Workshop on Hyperspectral Image and Signal Processing: Evolution in Remote Sensing*, pp. 1–4, IEEE, 2010.

[14] R. Heylen, D. Burazerovic, and P. Scheunders, "Fully constrained least squares spectral unmixing by simplex projection," *IEEE Transactions on Geoscience and Remote Sensing*, vol. 49, no. 11, pp. 4112–4122, 2011.

[15] L. Wang, D. Liu, and Q. Wang, "Geometric method of fully constrained least squares linear spectral mixture analysis," *IEEE Transactions on Geoscience and Remote Sensing*, vol. 51, no. 6, pp. 3558–3566, 2013.

[16] G. Martin, V. González-Ruiz, A. Plaza, J. P. Ortiz, and I. García, "Impact of jpeg2000 compression on endmember extraction and unmixing of remotely sensed hyperspectral data," *Journal of Applied Remote Sensing*, vol. 4, no. 1, pp. 041796–041796, 2010.

[17] E. Christophe, "Hyperspectral data compression tradeoff," in *Optical Remote Sensing*, pp. 9–29, Springer, 2011.

[18] D. L. Donoho, "Compressed sensing," *IEEE Transactions on information theory*, vol. 52, no. 4, pp. 1289–1306, 2006.

[19] E. J. Candès *et al.*, "Compressive sampling," in *Proceedings of the international congress of mathematicians*, vol. 3, pp. 1433–1452, Madrid, Spain, 2006.

[20] D. Kittle, K. Choi, A. Wagadarikar, and D. J. Brady, "Multiframe image estimation for coded aperture snapshot spectral imagers," *Applied Optics*, vol. 49, no. 36, pp. 6824–6833, 2010.

[21] P. Vaidyanathan, "Generalizations of the sampling theorem: Seven decades after nyquist," *IEEE Transactions on Circuits and Systems I: Fundamental Theory and Applications*, vol. 48, no. 9, pp. 1094–1109, 2001.

[22] E. J. Candes and T. Tao, "Near-optimal signal recovery from random projections: Universal encoding strategies?," *IEEE transactions on information theory*, vol. 52, no. 12, pp. 5406–5425, 2006.

[23] J. Romberg, "Imaging via compressive sampling [introduction to compressive sampling and recovery via convex programming]," *IEEE Signal Processing Magazine*, vol. 25, no. 2, pp. 14–20, 2008.

[24] M. F. Duarte, M. A. Davenport, D. Takhar, J. N. Laska, T. Sun, K. E. Kelly, R. G. Baraniuk, *et al.*, "Single-pixel imaging via compressive sampling," *IEEE Signal Processing Magazine*, vol. 25, no. 2, p. 83, 2008.

[25] J. A. Tropp, M. B. Wakin, M. F. Duarte, D. Baron, and R. G. Baraniuk, "Random filters for compressive sampling and reconstruction," in *2006 IEEE International Conference on Acoustics Speech and Signal Processing Proceedings*, vol. 3, pp. III–III, IEEE, 2006.

[26] E. Candes and J. Romberg, "Sparsity and incoherence in compressive sampling," *Inverse problems*, vol. 23, no. 3, p. 969, 2007.

[27] R. John, D. J. Brady, R. M. Willett, M. Gehm, and T. J. Schulz, "A snap-shot dual-disperser imager for compressive hyperspectral imaging," in *Frontiers in Optics*, p. FThG3, Optical Society of America, 2007.

[28] X. Lin, G. Wetzstein, Y. Liu, and Q. Dai, "Dual-coded compressive hyperspectral imaging," *Optics letters*, vol. 39, no. 7, pp. 2044–2047, 2014.

[29] H. Arguello and G. R. Arce, "Colored coded aperture design by concentration of measure in compressive spectral imaging," *IEEE Transactions on Image Processing*, vol. 23, no. 4, pp. 1896–1908, 2014.

[30] H. Rueda, H. Arguello, and G. R. Arce, "Dmd-based implementation of patterned optical filter arrays for compressive spectral imaging," *JOSA A*, vol. 32, no. 1, pp. 80–89, 2015.

[31] C. V. Correa, H. Arguello, and G. R. Arce, "Snapshot colored compressive spectral imager," *JOSA A*, vol. 32, no. 10, pp. 1754–1763, 2015.

[32] X. Lin, Y. Liu, J. Wu, and Q. Dai, "Spatial-spectral encoded compressive hyperspectral imaging," *ACM Transactions on Graphics (TOG)*, vol. 33, no. 6, p. 233, 2014.

[33] N. A. TREATY, "Survey of hyperspectral and multispectral imaging technologies," 2007.

[34] H. Arguello and G. R. Arce, "Code aperture optimization for spectrally agile compressive imaging," *JOSA A*, vol. 28, no. 11, pp. 2400–2413, 2011.

[35] H. Arguello and G. R. Arce, "Rank minimization code aperture design for spectrally selective compressive imaging," *IEEE Transactions on Image Processing*, vol. 22, no. 3, pp. 941–954, 2013.

[36] E. J. Candes, J. K. Romberg, and T. Tao, "Stable signal recovery from incomplete and inaccurate measurements," *Communications on pure and applied mathematics*, vol. 59, no. 8, pp. 1207–1223, 2006.

[37] E. J. Candes, Y. C. Eldar, D. Needell, and P. Randall, "Compressed sensing with coherent and redundant dictionaries," *Applied and Computational Harmonic Analysis*, vol. 31, no. 1, pp. 59–73, 2011.

[38] R. Berinde, A. C. Gilbert, P. Indyk, H. Karloff, and M. J. Strauss, "Combining geometry and combinatorics: A unified approach to sparse signal recovery," in *Communication, Control, and Computing, 2008 46th Annual Allerton Conference on*, pp. 798–805, IEEE, 2008.

[39] D. L. Donoho and M. Elad, "Optimally sparse representation in general (nonorthogonal) dictionaries via 1 minimization," *Proceedings of the National Academy of Sciences*, vol. 100, no. 5, pp. 2197–2202, 2003.

[40] W. Lu, W. Li, K. Kpalma, and J. Ronsin, "Near-optimal binary compressed sensing matrix," *arXiv preprint arXiv:1304.4071*, 2013.

[41] D. L. Donoho, M. Elad, and V. N. Temlyakov, "Stable recovery of sparse overcomplete representations in the presence of noise," *IEEE Transactions on information theory*, vol. 52, no. 1, pp. 6–18, 2006.

[42] M.-D. Iordache, J. M. Bioucas-Dias, and A. Plaza, "Sparse unmixing of hyperspectral data," *IEEE Transactions on Geoscience and Remote Sensing*, vol. 49, no. 6, pp. 2014–2039, 2011.

[43] A. Ramirez, G. R. Arce, and B. M. Sadler, "Spectral image unmixing from optimal coded-aperture compressive measurements," *IEEE Transactions on Geoscience and Remote Sensing*, vol. 53, no. 1, pp. 405–415, 2015.

[44] S.-J. Kim, K. Koh, M. Lustig, S. Boyd, and D. Gorinevsky, "An interior-point method for large-scale-regularized least squares," *IEEE journal of selected topics in signal processing*, vol. 1, no. 4, pp. 606–617, 2007.

[45] M. V. Afonso, J. M. Bioucas-Dias, and M. A. Figueiredo, "Fast image recovery using variable splitting and constrained optimization," *IEEE Transactions on Image Processing*, vol. 19, no. 9, pp. 2345–2356, 2010.

[46] M. V. Afonso, J. M. Bioucas-Dias, and M. A. Figueiredo, "An augmented lagrangian approach to the constrained optimization formulation of imaging inverse problems," *IEEE Transactions on Image Processing*, vol. 20, no. 3, pp. 681–695, 2011.

[47] S. Boyd, N. Parikh, E. Chu, B. Peleato, and J. Eckstein, "Distributed optimization and statistical learning via the alternating direction method of multipliers," *Foundations and Trends® in Machine Learning*, vol. 3, no. 1, pp. 1–122, 2011.

[48] M.-D. Iordache, J. M. Bioucas-Dias, and A. Plaza, "Total variation spatial regularization for sparse hyperspectral unmixing," *IEEE Transactions on Geoscience and Remote Sensing*, vol. 50, no. 11, pp. 4484–4502, 2012.

[49] J. M. Nascimento and J. M. Dias, "Vertex component analysis: A fast algorithm to unmix hyperspectral data," *IEEE transactions on Geoscience and Remote Sensing*, vol. 43, no. 4, pp. 898–910, 2005.

# Bibliography

A. Plaza, J. A. Benediktsson, J. W. Boardman, J. Brazile, L. Bruzzone, G. Camps- Valls, J. Chanussot, M. Fauvel, P. Gamba, A. Gualtieri, et al., "Recent advances in techniques for hyperspectral image processing," Remote sensing of environment, vol. 113, pp. S110–S122, 2009.

A. Ramirez, G. R. Arce, and B. M. Sadler, "Spectral image unmixing from optimal coded-aperture compressive measurements," IEEE Transactions on Geoscience and Remote Sensing, vol. 53, no. 1, pp. 405–415, 2015.

A. Wagadarikar, R. John, R. Willett, and D. Brady, "Single disperser design for coded aperture snapshot spectral imaging," Applied optics, vol. 47, no. 10, pp. B44– B51, 2008.

C. V. Correa, H. Arguello, and G. R. Arce, "Snapshot colored compressive spectral imager," JOSA A, vol. 32, no. 10, pp. 1754–1763, 2015.

D. J. Brady, Optical imaging and spectroscopy. John Wiley & Sons, 2009.

D. Kittle, K. Choi, A. Wagadarikar, and D. J. Brady, "Multiframe image estima- tion for coded aperture snapshot spectral imagers," Applied Optics, vol. 49, no. 36, pp. 6824–6833, 2010.

D. L. Donoho and M. Elad, "Optimally sparse representation in general (nonorthog- onal) dictionaries via 1 minimization," Proceedings of the National Academy of Sci- ences, vol. 100, no. 5, pp. 2197–2202, 2003.

D. L. Donoho, "Compressed sensing," IEEE Transactions on information theory, vol. 52, no. 4, pp. 1289–1306, 2006.

D. L. Donoho, M. Elad, and V. N. Temlyakov, "Stable recovery of sparse overcomplete representations in the presence of noise," IEEE Transactions on information theory, vol. 52, no. 1, pp. 6–18, 2006.

E. Candes and J. Romberg, "Sparsity and incoherence in compressive sampling," Inverse problems, vol. 23, no. 3, p. 969, 2007.

E. Christophe, "Hyperspectral data compression tradeo ," in Optical Remote Sensing, pp. 9–29, Springer, 2011.

E. J. Candes and T. Tao, "Near-optimal signal recovery from random projections: Universal encoding strategies?," IEEE transactions on information theory, vol. 52, no. 12, pp. 5406–5425, 2006.

E. J. Candès et al., "Compressive sampling," in Proceedings of the international congress of mathematicians, vol. 3, pp. 1433–1452, Madrid, Spain, 2006.

E. J. Candes, J. K. Romberg, and T. Tao, "Stable signal recovery from incomplete and inaccurate measurements," Communications on pure and applied mathematics, vol. 59, no. 8, pp. 1207–1223,

2006.

E. J. Candes, Y. C. Eldar, D. Needell, and P. Randall, “Compressed sensing with coherent and redundant dictionaries,” Applied and Computational Harmonic Analysis, vol. 31, no. 1, pp. 59–73, 2011.

G. Martin, V. González-Ruiz, A. Plaza, J. P. Ortiz, and I. García, “Impact of jpeg2000 compression on endmember extraction and unmixing of remotely sensed hyperspectral data,” Journal of Applied Remote Sensing, vol. 4, no. 1, pp. 041796–041796, 2010.

H. Arguello and G. R. Arce, “Code aperture optimization for spectrally agile com- pressive imaging,” JOSA A, vol. 28, no. 11, pp. 2400–2413, 2011.

H. Arguello and G. R. Arce, “Colored coded aperture design by concentration of measure in compressive spectral imaging,” IEEE Transactions on Image Processing, vol. 23, no. 4, pp. 1896–1908, 2014.

H. Arguello and G. R. Arce, “Rank minimization code aperture design for spectrally selective compressive imaging,” IEEE Transactions on Image Processing, vol. 22, no. 3, pp. 941–954, 2013.

H. Rueda, H. Arguello, and G. R. Arce, “Dmd-based implementation of patterned optical lter arrays for compressive spectral imaging,” JOSA A, vol. 32, no. 1, pp. 80– 89, 2015.

J. A. Tropp, M. B. Wakin, M. F. Duarte, D. Baron, and R. G. Baraniuk, “Random lters for compressive sampling and reconstruction,” in 2006 IEEE International Conference on Acoustics Speech and Signal Processing Proceedings, vol. 3, pp. III–III, IEEE, 2006.

J. M. Nascimento and J. M. Dias, “Vertex component analysis: A fast algorithm to unmix hyperspectral data,” IEEE transactions on Geoscience and Remote Sensing, vol. 43, no. 4, pp. 898–910, 2005.

J. Romberg, “Imaging via compressive sampling [introduction to compressive sam- pling and recovery via convex programming],” IEEE Signal Processing Magazine, vol. 25, no. 2, pp. 14–20, 2008.

L. Wang, D. Liu, and Q. Wang, “Geometric method of fully constrained least squares linear spectral mixture analysis,” IEEE Transactions on Geoscience and Remote Sens- ing, vol. 51, no. 6, pp. 3558–3566, 2013.

M. Breuer and J. Albertz, “Geometric correction of airborne whiskbroom scanner imagery using hybrid auxiliary data,” International Archives of Photogrammetry and Remote Sensing, vol. 33, no. B3/1; PART 3, pp. 93–100, 2000.

M. F. Duarte, M. A. Davenport, D. Takhar, J. N. Laska, T. Sun, K. E. Kelly, R. G. Baraniuk, et al., “Single-pixel imaging via compressive sampling,” IEEE Signal Pro- cessing Magazine, vol. 25, no. 2, p. 83, 2008.

M. Gehm, M. Kim, C. Fernandez, and D. Brady, “High-throughput, multiplexed pushbroom hyperspectral microscopy,” Optics express, vol. 16, no. 15, pp. 11032– 11043, 2008.

M. J. Golay, “Multi-slit spectrometry,” JOSA, vol. 39, no. 6, pp. 437–444, 1949. 41

M. Parente and A. Plaza, “Survey of geometric and statistical unmixing algorithms for hyperspectral images,” in 2010 2nd Workshop on Hyperspectral Image and Signal Processing: Evolution in Remote Sensing, pp. 1–4, IEEE, 2010.

M. V. Afonso, J. M. Bioucas-Dias, and M. A. Figueiredo, “An augmented lagrangian approach to the constrained optimization formulation of imaging inverse problems,” IEEE Transactions on Image Processing, vol. 20, no. 3, pp. 681–695, 2011.

M. V. Afonso, J. M. Bioucas-Dias, and M. A. Figueiredo, “Fast image recovery us- ing variable splitting and constrained optimization,” IEEE Transactions on Image Processing, vol. 19, no. 9, pp. 2345–2356, 2010.

M.-D. Iordache, J. M. Bioucas-Dias, and A. Plaza, “Sparse unmixing of hyperspectral data,” IEEE Transactions on Geoscience and Remote Sensing, vol. 49, no. 6, pp. 2014– 2039, 2011.

M.-D. Iordache, J. M. Bioucas-Dias, and A. Plaza, “Total variation spatial regular- ization for sparse hyperspectral unmixing,” IEEE Transactions on Geoscience and Remote Sensing, vol. 50, no. 11, pp. 4484–4502, 2012.

N. A. TREATY, “Survey of hyperspectral and multispectral imaging technologies,” 2007.

N. Gat, “Imaging spectroscopy using tunable lters: a review,” in AeroSense 2000, pp. 50–64, International Society for Optics and Photonics, 2000.

N. Keshava and J. F. Mustard, “Spectral unmixing,” IEEE signal processing maga- zine, vol. 19, no. 1, pp. 44–57, 2002.

N. Keshava, “A survey of spectral unmixing algorithms,” Lincoln Laboratory Journal, vol. 14, no. 1, pp. 55–78, 2003.

P. Vaidyanathan, “Generalizations of the sampling theorem: Seven decades after nyquist,” IEEE Transactions on Circuits and Systems I: Fundamental Theory and Applications, vol. 48, no. 9, pp. 1094–1109, 2001.

R. Berinde, A. C. Gilbert, P. Indyk, H. Karlo , and M. J. Strauss, “Combining geometry and combinatorics: A uni ed approach to sparse signal recovery,” in Com- munication, Control, and Computing, 2008 46th Annual Allerton Conference on, pp. 798–805, IEEE, 2008.

R. Heylen, D. Burazerovic, and P. Scheunders, “Fully constrained least squares spec- tral unmixing by simplex projection,” IEEE Transactions on Geoscience and Remote Sensing, vol. 49, no. 11, pp. 4112–4122, 2011.

R. John, D. J. Brady, R. M. Willett, M. Gehm, and T. J. Schulz, “A snap-shot dual-disperser imager for compressive hyperspectral imaging,” in Frontiers in Optics, p. FThG3, Optical Society of America, 2007.

R. O. Green, M. L. Eastwood, C. M. Sarture, T. G. Chrien, M. Aronsson, B. J. Chip- pendale, J. A. Faust, B. E. Pavri, C. J. Chovit, M. Solis, et al., “Imaging spectroscopy and the airborne

visible/infrared imaging spectrometer (aviris),” Remote Sensing of Environment, vol. 65, no. 3, pp. 227–248, 1998.

S. Boyd, N. Parikh, E. Chu, B. Peleato, and J. Eckstein, “Distributed optimization and statistical learning via the alternating direction method of multipliers,” Founda- tions and Trends® in Machine Learning, vol. 3, no. 1, pp. 1–122, 2011.

S.-J. Kim, K. Koh, M. Lustig, S. Boyd, and D. Gorinevsky, “An interior-point method for large-scale-regularized least squares,” IEEE journal of selected topics in signal processing, vol. 1, no. 4, pp. 606–617, 2007.

W. L. Smith, D. K. Zhou, F. W. Harrison, H. E. Revercomb, A. M. Larar, H.-L. Huang, and B. Huang, “Hyperspectral remote sensing of atmospheric pro les from satellites and aircraft,” in Second International Asia-Paci c Symposium on Remote Sensing of the Atmosphere, Environment, and Space, pp. 94–102, International Society for Optics and Photonics, 2001.

W. Lu, W. Li, K. Kpalma, and J. Ronsin, “Near-optimal binary compressed sensing matrix,” arXiv preprint arXiv:1304.4071, 2013.

X. Lin, G. Wetzstein, Y. Liu, and Q. Dai, “Dual-coded compressive hyperspectral imaging,” Optics letters, vol. 39, no. 7, pp. 2044–2047, 2014.

X. Lin, Y. Liu, J. Wu, and Q. Dai, “Spatial-spectral encoded compressive hyper- spectral imaging,” ACM Transactions on Graphics (TOG), vol. 33, no. 6, p. 233, 2014.

Y. Guan, S. Guo, Y. Xue, J. Liu, and X. Zhang, “Application of airborne hyper- spectral data for precise agriculture,” in Geoscience and Remote Sensing Symposium, 2004. IGARSS’04. Proceedings. 2004 IEEE International, vol. 6, pp. 4195–4198, Ieee, 2004.